REGULAR PAPER

Dexterity, Workspace and Performance Analysis of the Conceptual Design of a Novel Three-legged, Redundant, Lightweight, Compliant, Serial-parallel Robot

David Feller[1]

Abstract

In this article, the mechanical design and analysis of a novel three-legged, agile robot with passively compliant 4-degrees-of-freedom legs, comprising a hybrid topology of serial, planar and spherical parallel structures, is presented. The design aims to combine the established principle of the Spring Loaded Inverted Pendulum model for energy efficient locomotion with the accuracy and strength of parallel mechanisms for manipulation tasks. The study involves several kinematics and Jacobian based analyses that specifically evaluate the application of a non-overconstrained spherical parallel manipulator as a robot hip joint, decoupling impact forces and actuation torques, suitable for the requirements of legged locomotion. The dexterity is investigated with respect to joint limits and workspace boundary contours, showing that the mechanism stays well conditioned and allows for a sufficient range of motion. Based on the functional redundancy of the constrained serial-parallel architecture it is furthermore revealed that the robot allows for the exploitation of optimal leg postures, resulting in the possible optimization of actuator load distribution and accuracy improvements. Consequently, the workspace of the robot torso as additional end-effector is investigated for the possible application of object manipulation tasks. Results reveal the existence of a sufficient volume applicable for spatial motion of the torso in the statically stable tripodal posture. In addition, a critical load estimation is derived, which yields a posture dependent performance index that evaluates the risks of overload situations for the individual actuators.

1 Introduction

The research on the legged locomotion of robots has given rise to many different mechanical designs, motivated by a wide range of specific applications and goals that should be accomplished by the legged robot. For instance, different objectives may involve fast running, high load-carrying capacity, locomotion over uneven terrain or the requirement to perform additional and accurate manipulation tasks. However, a more general distinction can be made by considering multiple central aspects of the robot morphology and its consequences, like the number of legs, statically or dynami-cally stable locomotion, the employed gait, the inclusion of passive or active compliance inside the leg mechanism, the type of actuation and the topological layout of the mechanical assembly, which may feature a parallel, serial or hybrid arrangement.

With this work, the novel design of a legged robot as depicted in Fig. 1 is investigated that features the intricate combination of several specific design concepts as a measure to exploit their respective advantages to possibly yield a highly agile, fast and dextrous robot. Fundamentally, the design of the robot aims to combine agility, leg compliance and a torso centric mass distribution—as found in robots constructed with the Spring Loaded Inverted Pendulum (SLIP) [1] model in mind—with the stiffness, precision and strength of parallel mechanisms. Both domains are connected by the hybrid behaviour of the leg spring mechanism, which acts as a threshold between two possible task configurations of the robot. As such, accurate object manipulation may be per-

✉ David Feller
  david.feller@tu-clausthal.de

1 Institute of Electrical Information Technology, Clausthal University of Technology, Arnold-Sommerfeld-Str.1, Clausthal-Zellerfeld D-38678, Germany
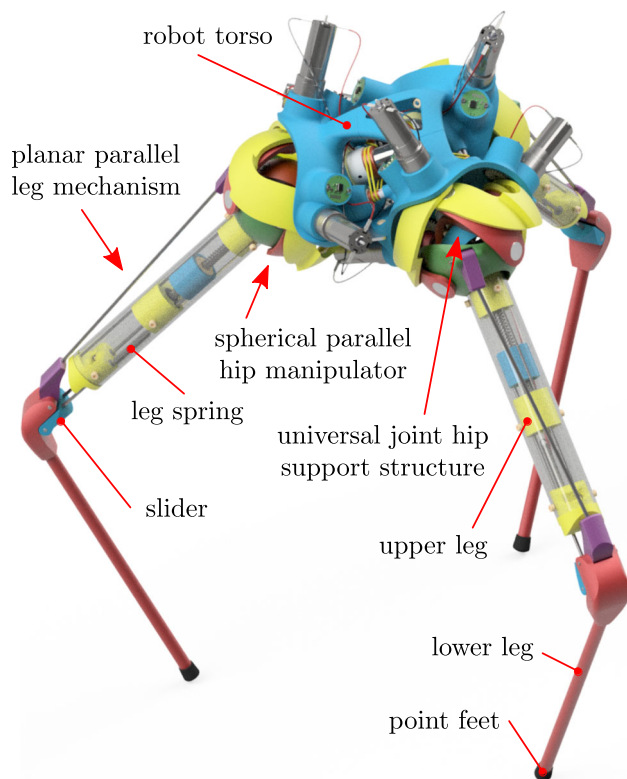
Fig. 1 CAD model of the prototype robot. The robot features three legs, a 3-DOF spherical hip joint, a 1-DOF knee joint, an additional DOF for the passive leg compliance and a serial-parallel actuation with 12 DC-motors, all located inside the robot torso. Both the hip mechanism and the upper leg comprise closed-loop linkages, connected in series along the leg

1.1 Robot Design Fundamentals

The design of the prototype robot, as discussed in this article, was introduced in general in our previous works [2] and [3]; however, the current version of the robot features some reworked and optimized components. Importantly, the robot design was driven by multiple aspects, which include the primary goal of energy efficient dynamic locomotion over uneven terrain (A), the ability to fast and responsively alter its posture (B) and the option to perform precise object manipulation (C). To accomplish these goals (A–C) in the future research, several decisions (I–V) were made regarding the design of the robot, as discussed in the following.

1.1.1 Three-Legged Design (I)

Many legged robots are constructed with an even number of legs, which mostly results in designs close to examples found in nature. Thus, most walking, running and jumping robots either feature two, four or six legs, as e.g. reviewed in [4]. In this regard, an even number of legs naturally yields symmetrical gaits due to groups of legs alternatingly performing swing and support phases. In addition, a large number of legs often allows for statically stable locomotion, as for example with hexapod robots, employing the tripod gait [5]. Static stability is possible due to the support polygon—spanned by the foot contact surfaces and the individual feet in contact with the ground surface—being large enough for either the projected center of mass (COM) or the zero moment point (ZMP) [6] to stay inside the polygon contour. Consequently, considering locomotion over uneven terrain, a larger number of legs thus allows for better general stability during traversal and often improved load carrying capacity, [4]. Hence, with fewer legs and increased movement speed, static stability becomes more challenging, which inevitably requires dynamically balanced locomotion as e.g. shown with the two-legged robots ATRIAS [7] or Cassie [8]. However, considering the vast literature of legged robots, there exist less examples of robots that explore architectures with an uneven number of legs, although multiple hopping robots, such as the Raibert Hopper [9] or Salto [10] show that movement is achievable with only one leg.

Thus, in this work, the design of a radial symmetrical three-legged robot is examined, which is an architecture researched in less depth than e.g. two or four legged systems. Naturally, a three-legged architecture imposes several difficulties regarding the solution to a feasible locomotion strategy, as walking stability and gait generation become more abstract problems due to the absence of biological templates. However, a three-legged system provides the min-

formed in the statically stable and stiff tripodal posture, while energy efficient dynamically balanced legged locomotion can possibly be achieved in the compliant state. Certainly, the intricate and mechanically complex approach has drawbacks on its own, as there are workspace limitations, several internal mechanical constraints, highly difficult kinematics and dynamics and the requirement for a sophisticated controller design to cope with the complexity of the robot. Still, the proposed robot may benefit from its respective design choices in such a way that it is able to sufficiently work and transitions between both tasks.

In this regard, the primary research contribution of this work is the analysis of the robot based on its kinematical behaviour with respect to dexterity, workspace and performance characteristics, being achieved with the proposed robot design. Consequently, these properties allow to evaluate the three-legged robot for its target application. In the following, the design fundamentals of the proposed robot and its conceptual ideas with respect to existing robots in the literature are introduced.

imum number of simultaneous ground contacts that allow for a statically stable pose, which might be exploited later on for accurate manipulation tasks, as targeted with goal (C). Furthermore, a minimal number of legs naturally reduces the total weight of the robot, which can benefit the goals (A) and (B), regarding energy efficiency and agility.

For reference, other robots with such an architecture are for example the three-legged robots in [11–19]. In particular, the robot STriDER in [11] contains four serially actuated joints per leg and flips its entire torso with each step. Thus, the robot is able to consecutively swing each leg to the other side of its own body to enter the next tripodal posture. In contrast, the robot Martian III in [12] has a fixed leg orientation, but varies the length of its legs by utilizing a linear actuator, allowing locomotion by oscillatory actuation. In [13], the static stability of the three-legged serial architecture was investigated by applying a predictive control method. A three-legged walk, turning a jumping movement was shown with the small three-legged robot Trinibot in [14], utilizing only three DC-motors in total with a RSSR loop mechanism, transforming motor rotation into leg swinging motion. The three-legged robot in [15] moves through application of oscillatory motions, and contains two servo motors per leg, corresponding to rotatory hip and linear leg joints. Notably, the actuators were kept outside of the leg structure to achieve high-speed motions. Interestingly, the robot from [15] specifically comprises springs, serially embedded into its legs, as required for its locomotion dynamics. Thus, the robot targets a resemblance of the SLIP model [1], which the proposed robot similarly constitutes through combination of leg compliance (IV) and specific mass distribution (V). A gait synthesis for a three-legged robot comprising three servo motors per leg based on a learning algorithm was shown in [16]. A parallel robot considered for machining tasks moving on a surface with three attachment points was investigated in [17]. Recently, the three-legged robot MARM (Multi-Arm Relocatable Manipulator) [18] was presented that is intended to use its limbs for walking, transporting payload and manipulation in space exploration. A current research project of the three-legged robot TriPed regarding novel locomotion methods is presented in [19].

However, the proposed legged robot presents several differences regarding certain mechanical properties, which are discussed with the additional methods (II–V). In particular, a serial leg architecture was employed in the robots [11–14, 16, 18], which stands in contrast to the serial-parallel design (II). Additionally, no explicit leg compliance (IV) was integrated into the robots [11–14, 16]; however, Martian III [12] allows some deformation of its legs, as required for its locomotion. In [17], the on-structure robot was designed with focus on high stiffness and rigidity. In contrast, the proposed robot in this article features three dedicated passive degrees-of-freedom (DOFs) utilized for its leg compliance (IV). Specifically, as locomotion (A, B) and object manipulation (C) are key properties of the proposed robot, in addition a certain dexterity and a reasonable workspace are required. This however is not a specific target for several aforementioned robots, which results in different properties. This is e.g. based on the reduced number of actuated joints in the robots Martian III [12], Trinibot [14] and the robots from [15, 17], or the small size of the robots from [14] and [15]. Thus, the robot presented is equipped with legs of a suitable length, allowing for a sufficient range of motion and features 12 active DOFs in total. The number of DOFs per leg creates an additional functional redundancy, possibly to be exploited for optimised motion execution, regarding dexterity and accuracy.

1.1.2 Serial-Parallel Mechanism Layout (II)

Considering the concept of actuation, many robots employ a mechanical design with the actuators being placed in serial order along the joints of the mechanism, which can be observed for example at the robots ANYmal [20] or MIT Cheetah 3 [21]. As such, a serial design has several advantages, which are mostly simple kinematic expressions and larger workspaces, in comparison to the more complex and constrained parallel architectures that often require involved mathematical solutions to their kinematics. However, serial designs can affect the agility of the robot, as actuators must accelerate masses and inertias of the follower actuators in a series arrangement, which may be a considerable drawback. Still, optimizations can be applied in serial architectures via the transmission of joint torques using linkages, belts or strings to optimize the location of the actuators as a measure to achieve lightweight legs, as seen for example with the Cheetah 2 [22] and 3 [21] robots.

On the contrary, legged robots that use parallel architectures—as in [7, 23–33]—may benefit from multiple advantages, such as improved accuracy, stiffness, strength and speed in comparison to conventional serial robots [34], which are aspects that may be exploited with respect to the design of agile legs. However, the application of parallel actuation in the field of legged robots is more uncommon [29, 35, 36] than serial actuation schemes. Still, robots with parallel actuation schemes are for example ATRIAS [7], HeritageBot [23], HexbotIV [24], Minitaur [25], Octopus [26], SpaceBok [27] or the parallel quadruped in [28]. From the aforementioned examples, several legged robots make use of the specific characteristics of parallel mechanisms, as e.g. the high payload capacity of the robot in [28], HexbotIV [24] and Octopus [26]. The high stiffness and accuracy of parallel mechanisms was put to use with the six-legged hole drilling robot in [29].

Yet, the exploitation of high agility and speed of parallel mechanisms can be observed at the leg design of the ATRIAS [7] robot.

Certainly, beside the requirement of elaborate control algorithms due to their mechanical complexity, practical drawbacks exist, as parallel robots are often compromised in their range of motion, which is the inherent consequence due to linkages, connected in closed loops. Interestingly, reconfigurable robot architectures, as e.g. shown in [17, 37], try to circumvent this disadvantage by altering their configuration to optimally correspond to the required task. In this sense, in [38] a legged robot with a novel single loop parallel leg mechanism with the advantage of a larger workspace was presented.

Aiming to combine the advantages of both domains, a hybrid serial-parallel architecture was employed, which consists of a parallel actuation for the robot hip joint and a serially connected actuation for the knee joint. Although being affected by an overall smaller workspace, the hybrid design allows for low inertia legs with a strong and precise hip actuation, while the series connection to the knee joint still provides a suitable range of motion. Considering the initial goals, as such, the speed of the parallel mechanism may benefit goal (B) regarding agility, while accuracy and stiffness may improve general manipulation tasks (C). In this regard, hybrid approaches in the design of robot legs can also be observed in the wall climbing robot from [39] and the four legged robot in [40]. Similarly, the possible advantages of the hybrid approach was considered in the leg design shown in [41] and the in-pipe peristaltic robot in [42]. In [43] hybrid mechanisms for bone surgery were investigated.

1.1.3 Non-Overconstrained Internal Load Support Structure (III)

The mechanical layout of the parallel structure used for the hip joints is specifically known as the spherical parallel mechanism (SPM) [44], which allows to create purely spherical motion of the end-effector relative to its base by three rotary actuators. A serial architecture providing a similar motion characteristic is the RRR structure, utilized e.g. in gimbal systems [45]. The SPM is vastly studied in the literature [44, 46–56]. Since the manipulator provides high accuracy, stiffness and speed, it is generally utilized as an orientation device. Hence, it was used to develop a camera orienting device—the Agile Eye [48, 51]—and is actively researched in the context of medical and surgery applications, as discussed in the recent works [57–65]. Additionally, it was investigated as a hip exoskeleton device in [66]. A wrist exoskeleton device for force interaction was proposed in [67]. In [68] the SPM was used for the design of a prosthetic wrist. A self-balancing platform was designed in [69]. However, its application as a spherical hip manipulator for the purpose of legged locomotion of robots has received only minor research attention in the past. Thus, examples of robots that utilize the SPM are the two legged robot in [70, 71] and the four-legged robot in [40, 72]. However, the distinct usage of the SPM regarding a robot that focusses on a lightweight and agile design was not further investigated, except the initial research in our previous works [2, 3].

In general, the linkages of a parallel mechanism must transmit both forces and torques between base and end-effector. Regarding its application in this work as the hip joint in a legged robot, naturally, it is a highly stressed part that must resist large static or dynamic forces and impacts. Furthermore, certain postures of the parallel manipulator can lead to a single linkage being loaded exceedingly more than the other linkages, which might cause problems regarding the rigidity of the mechanical parts.

Specifically, in the context of a spatially miniaturized and lightweight manipulator as integrated into the robot presented—which must keep a low total mass to achieve high agility (B)—the physical size of the linkages and their material properties are limiting factors. Fundamentally, the linkage cannot occupy a larger space due to otherwise possible mechanical collisions with neighbouring parts. Thus, a functional separation was employed, redirecting forces and torques onto different mechanical structures as a measure to reduce the load on the linkages, as the general SPM is not suitable regarding the force transmission demands in this specific application.

Consequently, a non-overconstrained design was used for the hip joint, comprising an outer parallel mechanism for the joint actuation, and an inner force absorbing central universal joint like support structure. By this measure, which alters the general SPM structure, the load exerted on the parallel linkages of the hip mechanism is lowered substantially, [2]. Particularly, this addition was not present in the legged robots utilizing the SPM from [70, 71] and [40, 72]. As a measure to keep the mechanical system non-overconstrained—which is required to specifically distribute forces and torques inside the system—the typical SPM that features a 3-RRR layout was replaced with the 6-DOF 3-CCC layout, which is prevented from falling apart by the internal RRR support structure. In this regard, the non-overconstrained design allows for a spatially small, yet robust construction.

1.1.4 Leg Compliance (IV)

With regard to efficient and dynamically balanced walking and running, leg compliance plays a crucial role [73] in many robotic designs, as this allows for storing and releas-

ing energy during the locomotion cycle. Compliance can be achieved by the integration of elastic elements, which are often implemented independently from the chosen actuation concept, as elasticities are typically connected in series to the actuated joints. Alternatively, compliance is achievable via software as part of the motor control algorithm as e.g. employed in virtual model control (VMC) [74], mimicking the behaviour of actual elastic components. Consequently, a series elasticity was integrated into the leg mechanism as important component regarding energy efficient locomotion as targeted with goal (A).

Notably, the integration of the spring in the case of the specific leg design of the proposed robot is more complicated than with robots that employ a more simple mechanism. Specifically, the integration of elasticities into the linkage structure of the leg mechanism itself is not advisable due to the highly nonlinear kinematic properties of the SPM. As a solution, the mechanical combination of two closed loop mechanisms in series with one common link was employed, additionally incorporating the underlying internal support structure (III). Importantly, as we demonstrated in our previous work [3], this yields a design with a reasonable linear behaviour of the resulting virtual leg spring, which acts between the robot feet and hip joints, and thus is a key design component of this robot.

Importantly, due to the specific mechanical realization of the leg compliance—involving pre-stressed springs—a hybrid behaviour was achieved, which keeps the robot in a stiff configuration, possibly benefiting accurate manipulation tasks (C). However, in motion, a threshold can be exceeded, which allows the legs to transition into a compliant state, as important for locomotion (A, B).

1.1.5 Concentrated Mass Distribution (V)

With the SLIP model [1]—which is studied in depth in the literature—being a fundamentally relevant concept regarding legged robots, a design that specifically captures a systemic closeness to this model may allow for agile and energy efficient dynamically balanced legged locomotion, as e.g. shown with ATRIAS [7].

Hence, a torso-centred, highly condensed mass distribution with legs that correspondingly comprise relatively low mass and inertia was a key design component of the robot presented. Consequently, combining the overall mass distribution with the compliance of the legs (IV), this may allow the application of control laws derived from the SLIP model and thus may benefit the realization of the goals (A) and (B). In particular, the realization of the dense mass concentration is directly coupled to the serial-parallel actuation (II), which allows for the distinctive location of the actuators.

1.2 Scope and Article Structure

Since the design of the hip joint is a central component in the proposed legged robot, this article focusses specifically on the resulting properties of the mechanism as the robot employs different postures. Fundamentally, the analyses in this article require the solution to the inverse kinematics of the robot model. However, the derivation of the extensive mathematical solution employed for the full robot model is beyond the scope of this paper. Nonetheless, a video of a motion execution is included in the supplementary materials, which shows the plausibility of the implementation. With this solution, the posture of the robot is completely defined by evaluation of the forward homogenous transformation calculations. Based on the resulting posture, the workspace is evaluated and several Jacobian based analyses are portrayed in this article. Thereby, the application of the proposed robot design for the tasks of legged locomotion and object manipulation is assessed.

The rest of the paper is organized as follows: First, Sec. 2 briefly discusses the mechanical structure of the robot, including details regarding the realization of the design methods

Fig. 2 Multi-body representation of the prototype robot. Abbreviations: Revolute (R), cylindrical (C), prismatic (P), constant velocity (CV), spherical (S), screw/helical (H), miniature belt transmission (T_B), helical gear transmission (T_H), linear transmission (T_L), proximal link (pl) and distal link (dl). Color legend for joint actuation: active (red), passive spring retraction force (blue). Green color marks axes that are equipped with angular or linear encoders
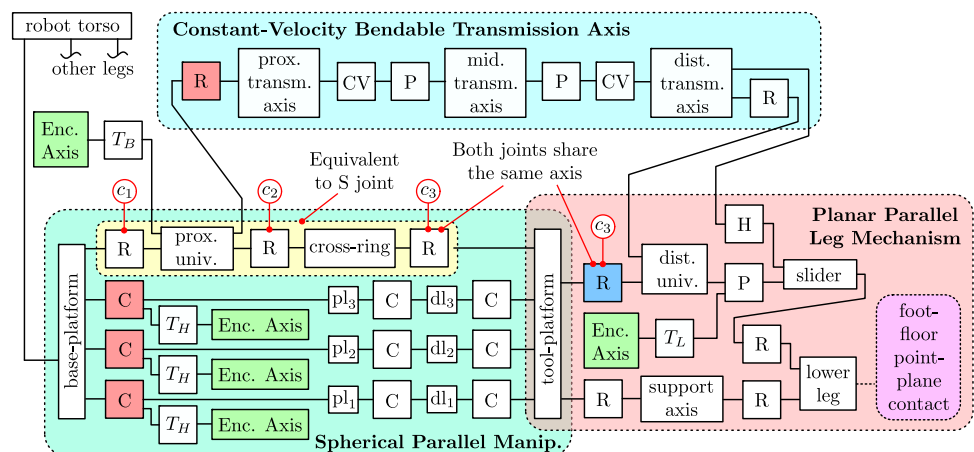
(I–V). Afterwards, the analysis of the SPM in the context of its application as a hip joint for the legged robot is performed, which focusses on the kinematic properties in Sec. 3 and on its performance evaluation in Sec. 4. Since this article features multiple analyses, each of them comprises an individual part that presents its results. Thus, Sec. 5 discusses and interprets the individual results, findings and their interrelation. Lastly, Sec. 6 draws a conclusion and Sec. 7 discusses future work.

2 The Prototype Robot

Fig. 1 displays the 3D model of the current legged robot prototype. The internal multi-body representation of rigid bodies and joints is depicted in Fig. 2, including the names of parts, joints and axes, referred to in this article. For a detailed discussion regarding the mechanical design, refer to the previous work [3]. In the figure, actively driven joints are marked with red color and passively driven ones—due to torque exerting elastic elements—are colored in blue. In addition, the connection of the sensor devices with their respective connection to the measured axes is displayed. In the following, the design of the robot is briefly discussed, stating how the design methods (I–V) are incorporated mechanically into the robot model.

2.1 Realization of the Design Methods (I–V)

Regarding design method (I), the robot consists of the central torso assembly and serial-parallel actuated legs, connected radial symmetrically. Each leg is connected with a spherical parallel hip manipulator driven by three actuators to the torso. In the depicted posture, the torso centre tray is located approximately 0.42 m above the ground level; hence, the robot is of rather small size.

Importantly, the legs themselves feature a planar parallel architecture, which both allows for the motion of the knee joint through the serial-parallel actuation (II) and for the compliant leg behaviour (IV). Specifically, each leg consists of a four-bar closed-loop mechanism, connecting tool platform and lower leg, with one bar being length-adjustable via a slider mechanism, which transforms rotation into translation through a screw joint. The slider screw axis is driven by the knee actuator, which is located inside the robot torso, connected via a constant velocity bendable transmission axis. This torque transmission axis goes through the centre of both the spherical parallel hip mechanism and the universal joint support structure, occupying the inner space of the mechanism. Hence, it was possible to both locate the motor inside the robot torso (V) and yet allow for a serial actuation (II) of the knee with respect to the hip actuation. This allows for lightweight legs, with the masses of the actuators placed completely outside of the moving structures.

The structural shape of the robot is built by combining thin aluminium parts with lightweight, yet reasonable rigid 3D printed parts and stiff off-the-shelf plastic tubes and axes. This allows for an overall functionally intricate design, resulting in a compact and highly interconnected construction. In this sense, as observable in the figures, a close interlocking arrangement was chosen, tightly arranging the set of 12 cylindrically shaped compact DC-motors without mechan-
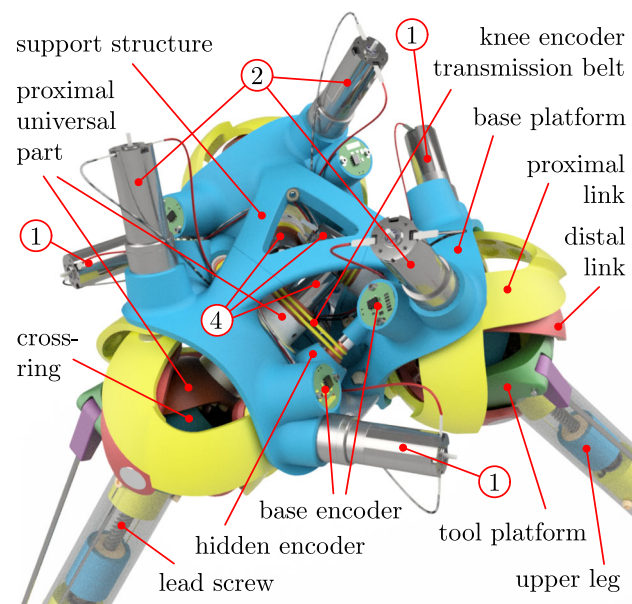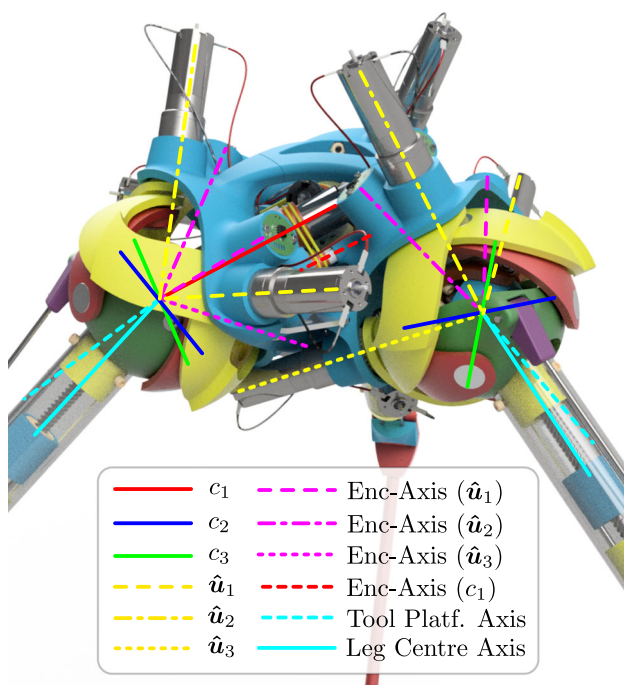

Fig. 3 Detail view of the upper side of the torso section of the robot model. The numbers depict the indices, used for the actuator axes in this article
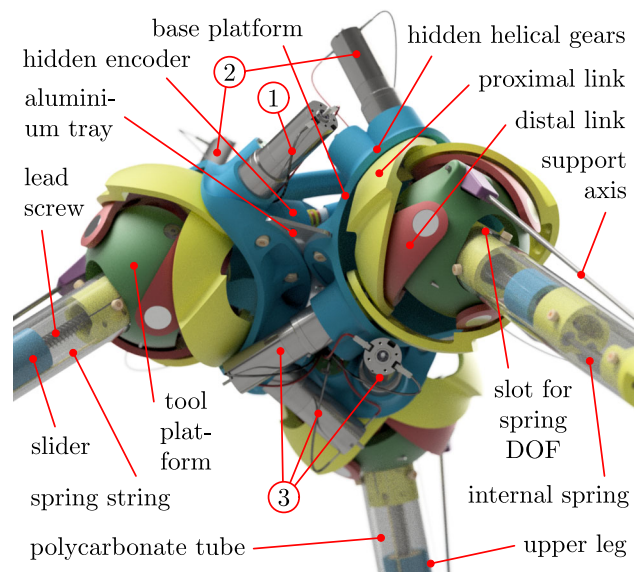
Fig. 4 Detail view of the robot torso section from below, depicting the close and collision free arrangement of the hip actuators

ical interference. Thus, concentrated in a narrow volume in the robot torso, the resulting centre of mass is located closely to the geometric centre of the robot torso, realizing design method (V). The location of the individual actuators is depicted in the Figs. 3, 4 and 5. Each actuator is distinguished in the rest of the article via an index number, which is 1-3 for the base actuators, and 4 for the knee actuator. In addition, Fig. 5 displays the notation for the axes vectors, referred to regularly in this article. For reference, a real-world prototype of one leg was built in the previous work, [3]. Essentially, the total weight of the robot—calculated from the CAD representation—measures only 3.407 kg, which is plausible based on the weight of the single built real world leg. Importantly, the combined weight of the 12 actuators holds 1.29 kg, which is approximately 37.9 % of the total robot mass. Consequently, the remaining mass taken by the robot skeleton structure is only a comparatively minor part of the whole assembly, and is considered as a rather important aspect with respect to the overall design of a legged robot [25, 75].

The hip joints are internally connected with a RRR universal joint structure in the inside of the spherical parallel

Fig. 5 Detail view of side of the torso section, showing the individual joint axes of the robot. Yellow lines depict the actuator axes and magenta lines the corresponding encoder axes. The transmission of the base actuator angular position is transferred via a helical gear connection to the three base encoders of each hip unit. A hidden redundant encoder marked with the red dashed line measures the axis orientation c_1 via the miniature transmission belt. The depiction of the hip joints reveals the force absorbing central universal joint structure in the centre of the SPM hip joints, with the axes c_1, c_2 and c_3 being marked with red, green and blue lines

actuated linkage structure, comprised of the joints c_1, c_2 and c_3. Thus, the inner support structure captures any forces introduced into the hip joint, which makes the universal joint structure equivalent to a passively connected spherical joint, while the outer spherical 3-CCC linkage structure—mechanically decoupled from the capability to engage with any forces introduced into the system—delivers the required joint torque. This combination of inner serial and outer parallel structure realizes the non-overconstrained hip mechanism from design method (III).

Importantly, the universal joint structure shares one revolute axis (c_3) with the four-bar mechanism of the leg, allowing the connection of two parallel mechanisms in series, with the tool platform being the common link. Crucially, this allows for the leg elasticity to be placed in series to the hip mechanism, circumventing the nonlinearty of the kinematics between the motion of the motor axes and the tool platform. Consequently, the leg compliance is realized by a spring that is embedded into the upper leg. The transmission of forces between the spring and the leg linkage is realized by a guided high strength string that specifically applies the retracting spring force between the lower side of the upper leg and the inner slot of the tool platform, which is equivalent to a torque applied at the shared axis c_3. Hence, with a prestressed spring, the transition from stiff to elastic behaviour requires to overcome a certain torque related, discrete threshold. Thus, the relative motion around this axis allows the leg to alter the shape of the planar four-bar linkage, changing the distance between foot and hip centre, depending on the force applied to the robot feet. This realizes the additional passive DOF required for the leg compliance from design method (IV).

Beside the actuation concept, sensors are integrated into the model to capture the current posture of the robot, as required for control algorithms. Each hip mechanism features three encoders for the base actuators. Additionally, a redundant encoder measures the angular position of the proximal universal joint part; thus, it measures the actual orientation of the knee actuator unit, which is able to rotate freely inside the torso assembly as depicted in the topological diagram. The slider position is measured with a miniature linear encoder located inside the cylindrically shaped tube of the upper leg.

2.2 The Hip Mechanism

For reference, a brief discussion of the general SPM is given in the following, which in addition serves as an introduction into the nomenclature that is specifically employed in this article.

Figure 6a shows a typical spherical parallel manipulator (SPM) with three linkages, comprised of proximal and distal link. Proximal links are connected via the actuator axis to
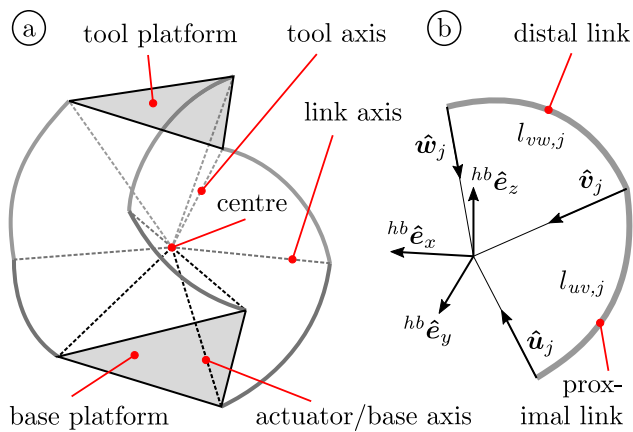
Fig. 6 (a) General layout of a spherical parallel manipulator with three parallel linkages connecting base and tool platform. All joint axes intersect in the common centre. (b) Layout of a single linkage structure, comprised of proximal and distal link

the fixed base platform of the manipulator and distal links are connected via the tool axis to the moving tool platform, which may correspond to the manipulator end-effector (EE). Proximal and distal links are joint via the link axis. All axes represent revolute or cylindrical joint axes and intersect in the centre of the SPM, which allows every part to rotate around this common point. Thus, the SPM acts as a 3-DOF spherical joint with the centre being the virtual point of rotation. By applying torque around the base axes, the orientation of the tool platform with respect to the base platform can be altered.

Figure 6b shows one constellation of link $j = 1, 2, 3$ of the mechanism inside the reference frame that is fixed to the base platform. In the context of the proposed prototype robot, the fixed frame is denoted with $\mathcal{F}_{hb}$ (hib base) as it corresponds to the part of the robot hip that is bound to the torso. Consequently, the reference frame local to the tool platform is denoted with $\mathcal{F}_{hf}$ (hip follower), as it has the role as the reference frame that follows after the application of spherical rotation. The origins of both frames intersect in the centre of the SPM. For each linkage structure j, comprised of the proximal link with arc length $l_{uv,j}$ and distal link with arc length $l_{vw,j}$, the actuator/base axis $\hat{\boldsymbol{u}}_j$ is fixed to the base platform, the tool axis $\hat{\boldsymbol{w}}_j$ fixed to the moving tool platform and the link axis $\hat{\boldsymbol{v}}_j$ connects proximal and distal links. All nine joint axes $\hat{\boldsymbol{u}}_j$, $\hat{\boldsymbol{v}}_j$, $\hat{\boldsymbol{w}}_j$ point to the origin of the base reference frame ($\mathcal{F}_{hb}$) and the follower reference frame ($\mathcal{F}_{hf}$) of the spherical hip joint, respectively, for each leg denoted with i. In this work, we use the optimal layout of the SPM, which is $l_{uv,j} = l_{vw,j} = \pi/2$ and $\pi/2$ between neighbouring axes of base and tool platforms.

The axes are referred to as the unit vectors $\hat{\boldsymbol{u}}_j$, $\hat{\boldsymbol{v}}_j$, $\hat{\boldsymbol{w}}_j$ in alphabetical order from the base to the tool platform. Notably, the naming convention regarding parts and the order of symbols $\hat{\boldsymbol{u}}_j$, $\hat{\boldsymbol{v}}_j$, $\hat{\boldsymbol{w}}_j$ regarding the joint axes was chosen for a consistent and logical style, thus it differs from notations often found in the literature regarding the general SPM.

3 Kinematics Analysis

One major aspect considering the implementation of the spherical parallel manipulator as the hip joint in the robot presented regards the orientation of base and tool platform of the mechanism, which is important considering possible actuator torque limitations, accuracy requirements and the mechanical feasibility. Thus, in the following, the motivations and consequences for selecting the specific hip configuration as depicted in the initial CAD Fig. 1 are discussed.

3.1 Orientation of the Reference Frames

As stated earlier, the parallel hip actuator scheme was chosen to achieve highly agile legs, with the robot mass centred and condensed in the robot torso. In this regard, the intention is to derive a robot design that functionally mimics the SLIP model closely. However, due to the spatial arrangement of the actuators and the inclusion of the leg compliance mechanism, a trade-off was required regarding the fundamental orientation the hip unit base platforms, as discussed in the following.

3.1.1 Orientation Trade-Off

As a result of the design intention, a spatially close arrangement using a series–parallel scheme regarding the 4-DOF actuation of the complete leg is only possible by orienting the base platforms in such a way that mechanical collisions between the cylindrically shaped actuators of neighbouring units are prevented. However, arbitrarily reorienting the base platforms will influence the achieved performance characteristics of the SPMs themselves, as the tool platform must compensate for the initially misaligned orientation. Thus, the results discussed in the following are derived from an iterative design process, keeping a structurally dense arrangement, yet a manipulator posture that is reasonably close to the ideal isotropic configuration in its intended workspace.

Furthermore, due to the series connection of both the hip and leg parallel mechanisms, which connects universal joint, tool platform, and upper leg through axis c_3, there exists an additional rotational freedom that the upper leg is able to perform on top of the tool platform. This DOF around axis c_3 is expressed by the spring slot angle φ_{spr} and is measured between the axis colinear with the upper leg and axis $^{hf}\hat{\boldsymbol{e}}_z$ vertical to the tool platform. The DOF is bounded mechanically by $\varphi_{spr} \in [-8°, +8°]$. In the default robot posture, due to the retracting spring force, the upper leg is pulled toward
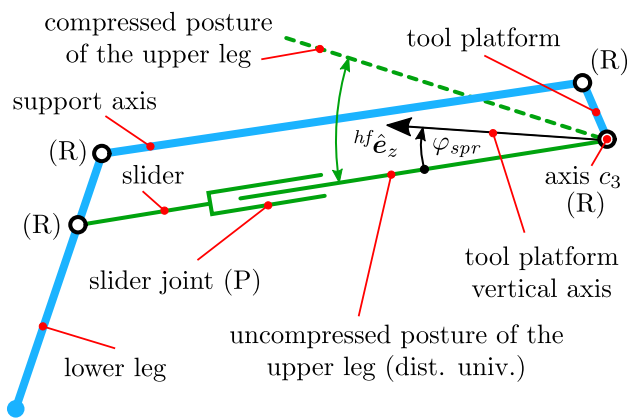
Fig. 7 Four-bar linkage of the leg mechanism, which accounts to the elastic compression of the leg. The φ_{spr} DOF allows for the reshaping of the closed-loop mechanism. Blue lines depict sides of fixed length. The green side is length adjustable via a prismatic slider, required for a controlled knee motion

the lower side of the tool platform slot, yielding the non-deflected leg position with $\varphi_{spr} = -8°$. Any deflection of φ_{spr} from this posture constitutes to an elastic compression of the leg, as this results in actively extending the internal spring via a guided string mechanism. Figure 7 depicts the leg mechanism graphically.

Consequently, the orientation of the tool platform is not only required to compensate for the specifically oriented base platforms—which is due to the close interlocking arrangement of the actuators—but it must in addition constitute for the leg compression DOF, requiring to rotate the tool platform upwards by 8° for the non-compressed leg state.
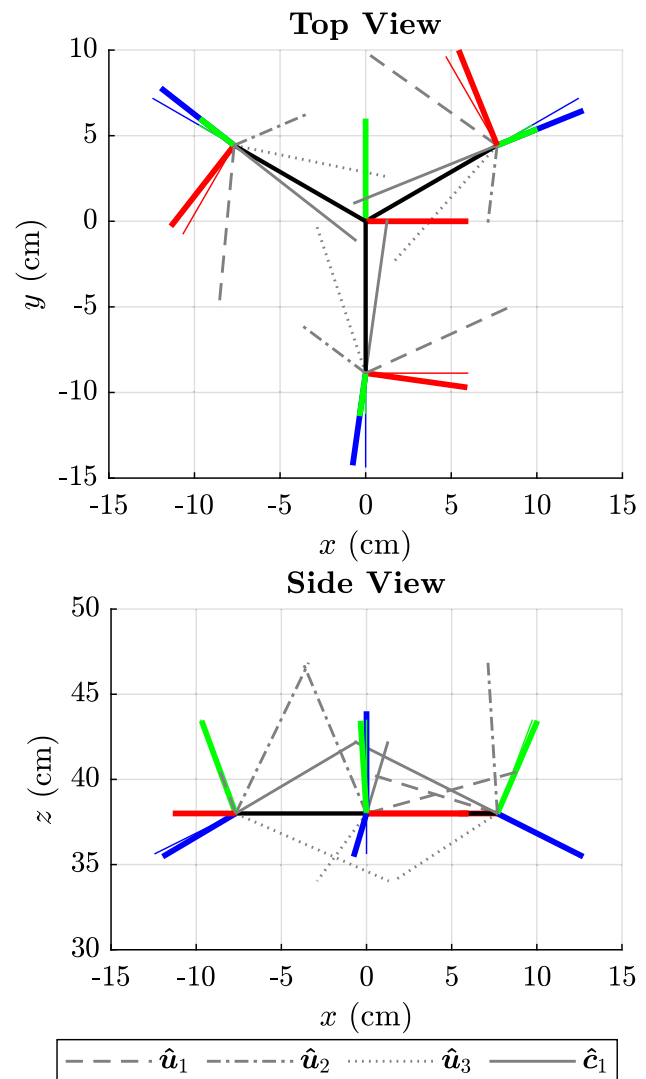
3.1.2 Final Structure

The final orientation of the hip units is expressed via the ZXZ-Euler angles in Table 1—accounting for the effects of the orientation trade-off—and is visually depicted including the actuator axes of the torso assembly in Fig. 8. The rotation

Fig. 8 Orthographic top view and side view of the hip unit base platform reference frames ($\mathcal{F}_{hb}$) and the resulting location of actuator axes. The viewing direction with respect to the torso centre reference frame reads $-\hat{e}_z$ (top) respectively $\hat{e}_y$ (side). Bold lines represent the $\mathcal{F}_{hb}$-frame, thin lines the $\mathcal{F}_{hf}$-frame

matrix built by the corresponding ZXZ-Euler angles determines the static orientation between the end-effector frame $\mathcal{F}_{ee}$, which is located and fixed in the torso centre and the individual hip base platform reference frames $\mathcal{F}_{hb}$. Note that the orientation of the $\mathcal{F}_{hf}$ frame depends on the current leg configuration or posture of the robot. Still, the vector along upper leg and lower leg lies always within the y-z-plane of the $\mathcal{F}_{hf}$ frame. This means that—in the default standing pose—the $\mathcal{F}_{hf}$ frame is always misaligned from the ideal location of the isotropic manipulator configuration, which is the effect of keeping the virtual leg plane vertical to the horizontal floor.

Table 1 ZXZ-Euler angles in degree of the hip base platform ($\mathcal{F}_{hb}$) and tool platform ($\mathcal{F}_{hf}$) reference frames in relation to the torso body reference frame $\mathcal{F}_{ee}$

i	$^{hb}_{ee}R$			$^{hf}_{ee}R$		
	Z_0	X_0	Z_1	Z_0	X_0	Z_1
1	112	115	0	120	113.36	0
2	−128	115	0	−120	113.36	0
3	−8	115	0	0	113.36	0
$^{hf}_{hb}R_i$		Z_0		X_0		Z_1
1-3		101.006		7.479		−104.288

Values for the $\mathcal{F}_{hf}$ frame are based on the standing pose with feet radius $r_f = 0.22$ m and torso height $h_t = 0.38$ m. The $\mathcal{F}_{hf}$ to $\mathcal{F}_{hb}$ Euler values are identical for each leg

3.1.3 Description of Orientation

The spherical motion of the tool platform against the base platform needs a mathematical expression, tailored to the specifics of robot model that is discussed in this article. Thus, the workspace and the motion capability of the manipulator can be described by three variables, namely vertical axis twist angle ϕ_v, tilt angle ϕ_t and rotation angle ϕ_r, respectively. Since the tool platform requires an initial orientation offset in the home configuration that is set for the robot model in its default pose, an additional in-between transformation matrix ${}^*_{hb}R$ is employed that is defined as:

$$ {}^{hf}_{hb}R_i = {}^*_{hb}R_i, \tag{1} $$

which means that in the home configuration, the orientation defined by the three variables ϕ_v, ϕ_t and ϕ_r relates to:

$$ {}^{hf}_*R_i = I \quad \text{for} \quad \phi_v = 0, \phi_t = 0, \phi_r = 0. \tag{2} $$

Thus, the twist angle ϕ_v is defined around the ${}^{hf}\hat{e}_z$ axis of the joint follower frame, the tilt motion by angle ϕ_t around a tilt axis ${}^*\hat{n}_t$ of the in-between frame and the rotation by angle ϕ_r around the ${}^*\hat{e}_y$ axis of the in-between frame. Therefore, the orientation of the tool platform can be expressed by the concatenation of the rotation matrices:

$$ {}^{hf}_{hb}R_i = {}^*_{hb}R_i \cdot {}^{hf}_*\left(R_n(\phi_{t,i}, {}^*\hat{n}_{t,i}) \cdot R_z(\phi_{v,i})\right) \tag{3} $$

with the tilt axis:

$$ {}^*\hat{n}_{t,i} = R_z(\phi_{r,i}) \cdot {}^*\hat{e}_{y,i} \tag{4} $$

for leg $i = 1, 2, 3$. In contrast to other possible statements for rotation, this expression has been chosen as being intuitive, since—assuming the SPM being in its initial configuration expressed by the rotation ${}^*_{hb}R_i$—Eq. 3 can be regarded as first twisting the tool platform around the vertical axis and afterwards tilting the tool platform simply towards the intended direction. The idea is that the actual twist of the SPM will not change significantly during locomotion of the robot model, whereas tilting motion will be utilized more frequently. This general trend was discovered also in the previous work [2] at the execution of simple motions and primitive locomotion, mainly utilizing tilt motions around an axis that is directed mostly horizontally to the floor plane. Thus, this works as the basic template for this analysis. Interestingly, the description for the orientation defined with Eq. 3 shares conceptual similarities to the Tilt-and-Torsion (T&T) expression of orientation, which was introduced earlier in [76–78].

An alternative expression of the orientation can be given by:

$$ {}^{hf}_{hb}R_i = R_n(c_1, \phi_z) R_n(c_2, \phi_y) R_n(c_3, \phi_x + \varphi_{spr}), \tag{5} $$

which resembles the actual orientation of the mechanical rotation axes of the joints included in the central universal joint like support construction, featuring the three axes c_1, c_2, c_3 with corresponding rotation angles ϕ_z, ϕ_y, ϕ_x. Refer to Fig. 2 for the depiction of the axes c_1, c_2, c_3 in the robot model. The angles ϕ_z, ϕ_y, ϕ_x are derived from the ZYX-Euler decomposition of the hip rotation matrix.

3.2 Dexterity and Accuracy

As the joint transformation matrix ${}^{hf}_{hb}R_i$ maps a vector between the follower and the base frame, so does the Jacobian matrix map joint rates into end-effector velocities. The Jacobian [79, p.149] of a mechanical system is defined in general as a linear mapping:

$$ \omega = J(\theta)\dot{\theta} \tag{6} $$

with the vector of linear and angular velocity ω of the tool-centre-point (TCP) or end-effector (EE) and the joint rates $\dot{\theta} = d\theta/dt$ with the generalized joint coordinates θ. In this case, ω equals the angular velocity vector of the tool platform and θ equals the angular positions of the actuator shafts in the base platform with $\theta = [\theta_1, \theta_2, \theta_3]^T$.

In [47, 51], it was shown that the equation:

$$ A\omega + B\dot{\theta} = 0 \tag{7} $$

with:

$$ A = \begin{bmatrix} (\hat{v}_1 \times \hat{w}_1)^T \\ (\hat{v}_2 \times \hat{w}_2)^T \\ (\hat{v}_3 \times \hat{w}_3)^T \end{bmatrix} \tag{8} $$

and with the diagonal matrix:

$$ B = \begin{bmatrix} (\hat{v}_1 \times \hat{u}_1) \cdot \hat{w}_1 & 0 & 0 \\ 0 & (\hat{v}_2 \times \hat{u}_2) \cdot \hat{w}_2 & 0 \\ 0 & 0 & (\hat{v}_3 \times \hat{u}_3) \cdot \hat{w}_3 \end{bmatrix} \tag{9} $$

leads to the construction of the Jacobian matrix J and its inverse J^{-1}, regarding Eqs. 6 and 7 by:

$$ J = -A^{-1}B \quad \text{and} \quad J^{-1} = -B^{-1}A. \tag{10} $$

As it was shown in our previous work [2], we will instead utilize the matrices X and Y with:

$$X = \begin{bmatrix} n_1 \ n_2 \ n_3 \end{bmatrix}, \tag{11}$$
$$Y = \mathrm{diag}\left(n_1 \cdot \hat{u}_1, \ n_2 \cdot \hat{u}_2, \ n_3 \cdot \hat{u}_3\right), \tag{12}$$

and with the vectors:

$$n_j = \hat{w}_j \times \hat{v}_j, \tag{13}$$

for computing the Jacobian J by:

$$J = X^{-T} Y \quad \text{and} \quad J^{-1} = Y^{-1} X^T. \tag{14}$$

For reference, Eq. 7 can be derived by differentiating the constraint equation of the kinematic loop closure expression with respect to the time. In contrast, the solution in Eq. 14 from our previous work was derived by observing the manipulator vector-moment propagation through its linkages, which yields a solution in the form of the torque input–output-relationship $\tau = J^T f$ of the manipulator with actuator torque vector τ and EE-torque vector f. Thus, the equation captures the same behaviour of the manipulator, but is derived by a geometric approach. While the equality of $-A$ and X^T is obvious, the equality of B and Y can be proven by the application of the vector triple product.

By relying on this solution, the problem formulation is shortened as it reuses the n_j vectors for both matrices X and Y, in contrast to the usually cited solution, which is formulated in e.g. [49]. However, since the matrices A, X and B, Y are just mathematical reformulations of the same expression, different notations can be found in the literature. For example, a similar notation to Eqs. 11 and 12, which also employs a compact form by sharing the same cross product terms in both matrices, was e.g. used previously in [53].

As shown in [51], while originally introduced in [80], the dexterity of a parallel manipulator can be expressed by the conditioning index $1/\kappa$, which is defined as the inverse of the condition number $\kappa(J)$ of the Jacobian matrix of the manipulator. It holds $1 \leq \kappa \leq \infty$ and $0 \leq 1/\kappa \leq 1$. The condition number $\kappa(J)$ is computed by:

$$\kappa(J) = \|J\| \left\| J^{-1} \right\| \tag{15}$$

and expresses—in the context of a robotic manipulator—the input–output-sensitivity of the mechanism to motion and forces. A conditioning index $1/\kappa$ of 1 corresponds to an isotropic configuration with ideal motion and force transmission and 0 corresponds to a singular configuration. The value of κ depends on the selected norm in Eq. 15; hence, for

Dexterity $1/\kappa$ over Workspace
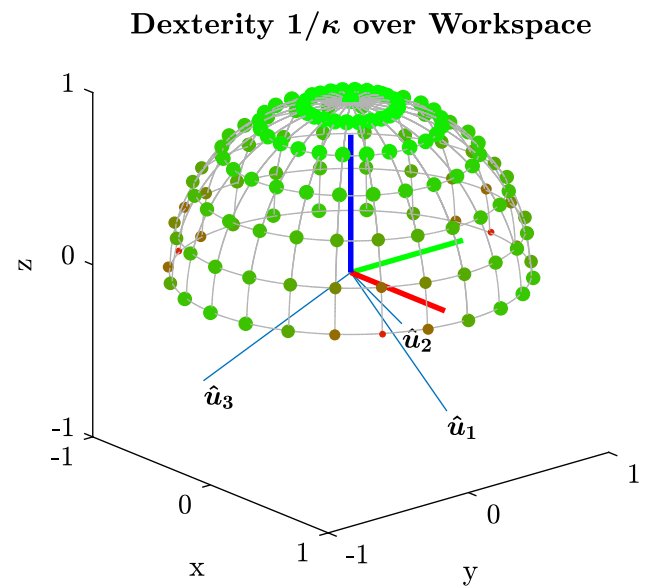
Fig. 9 Conditioning index $1/\kappa$ of the manipulator displayed as colored marker at different kinematical configurations. Each marker location corresponds to the intersection of the tilted $^{hf}\hat{e}_z$ axis with the unit sphere. The number is represented linear from 0 to 1 by red/small to green/big markers. The workspace is defined by $\phi_r \in [-\pi, +\pi]$, $\phi_t \in [0, \pi/2]$, $\phi_v = 0$. It holds $1/\kappa = 1$ at the central top position, depicting the manipulator isotropic pose

comparison reasons, the typically applied weighted Frobenius norm is used:

$$\|M\| = \sqrt{tr(M^T W M)}, \tag{16}$$

with the matrix $W = \frac{1}{n} I$ and n being the dimension of the applied matrix M. Since the Jacobian matrix J depends on the current configuration of the manipulator, the conditioning index is a local criteria. Figure 9 shows the resulting dexterity over different orientations of the manipulator with the twist angle $\phi_v = 0$ chosen for the best overall global conditioning index, which was derived in [46] as an integral of the local indexes over the manipulator workspace.

3.3 Analysis of Dexterity and Workspace

Regarding the specific robot model presented in this article, Fig. 10 depicts the conditioning index $1/\kappa$ for the misaligned default pose of the hip manipulator in the mechanical assembly. The conditioning index is displayed as colored dots on the grid of a half spherical shape, whose top position crosses the $^*e_z$ axis. Any point on the spherical grid depicts the intersection with the rotated $^{hf}e_z$-axis. Specifically, any rotation that is performed by the hip manipulator is expressed via Eq. 3; hence, the hemisphere is portrayed only via the vari-

Workspace Contour over Dexterity $1/\kappa$
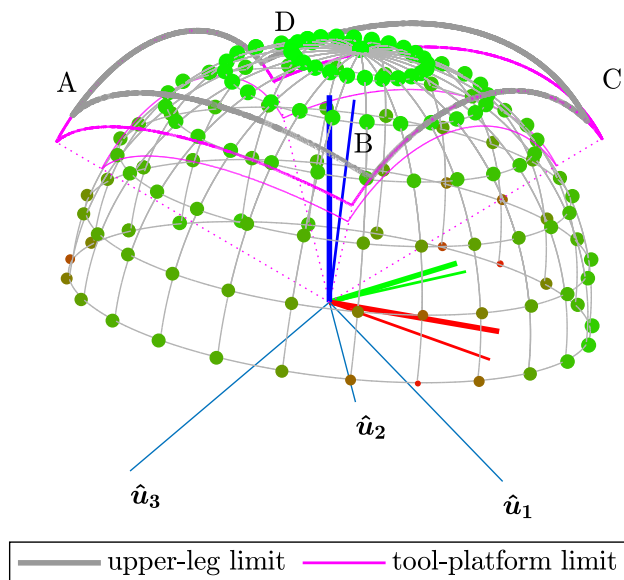
Fig. 10 Conditioning index displayed relative to the orientation in the robot default standing pose. Magenta and grey lines depict the reachable workspace borders. Letters A, B, C and D mark the corner points of the contour

Workspace Border Profiles
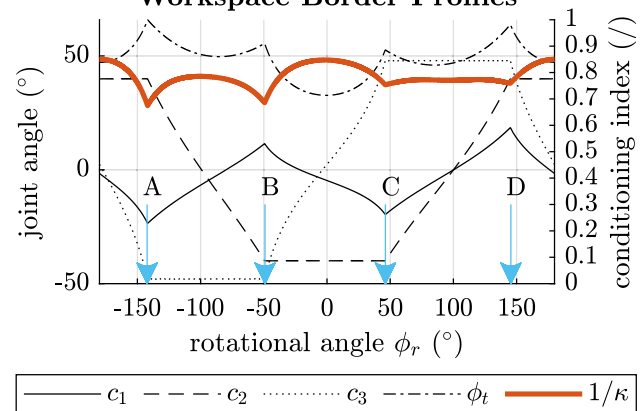
Fig. 11 Joint angles and conditioning index along the reachable workspace contour that is depicted as magenta line in Fig. 10. Letters A, B, C, and D depict the location of the corner points, which are marked in Fig. 10. In the diagram, the angle around axis c_3 contains the additional range due to the motion of the upper leg by the spring DOF angle φ_{spr}

ables ϕ_v, ϕ_t and ϕ_r, while the initial orientation offset is expressed via $^*_{hb}\boldsymbol{R}$. Since Fig. 10 depicts the default standing pose of the robot, Table 1 shows the Euler angle decomposition of this initial transformation matrix.

Due to the universal joint type central support structure, the orientation of the tool platform is limited towards a certain workspace. Table 2 shows the mechanical joint ranges for the involved axes. Thus, Fig. 10 depicts the workspace boundary curve presented as the three dimensional representation of any point, that is reachable by the $^{hf}\boldsymbol{e}_z$-axis during its motion inside the depicted hemisphere. Here, a distinction is made regarding the workspace contour of the upper leg (grey line) and the actual tool platform (magenta line), that is mounted on top. Thus, Fig. 10 visualizes the additional DOF around c_3 with φ_{spr} based on the spring slot rotation that is present for the tool platform with respect to the upper leg.

A different perspective on the subject is given with Fig. 11, which shows the joint angles at the axes c_1, c_2, c_3 of the universal type support structure along the workspace limit curve

Table 2 Joint ranges of the internal support structure, expressed through the axes c_1, c_2 and c_3 of the universal joint, defining the workspace of the robot hip joint

Ax.	Range	Ax.	Range	Ax.	Range
c_1	$[-45°, 45°]$	c_2	$[-40°, 40°]$	c_3	$[-40°, 40°]$

and the minimum values for the manipulator conditioning index $1/\kappa$ encountered in these configurations.

3.3.1 Results

From Fig. 10, it becomes visually apparent that the workspace contours are asymmetrically shaped due to the initial offset orientation of the tool platform. However, this distorts the symmetry of the manipulator conditioning index along its workspace contour, as depicted in Fig. 11. Still, as one can observe, the hip manipulator shows a well conditioned workspace, since the conditioning index along the workspace boundary—depicting the highest possible degradation from the ideal configuration—does not dip below 0.67 and has a median value of 0.77. In its default pose with $^{hf}_{hb}\boldsymbol{R} = {}^*_{hb}\boldsymbol{R}$, the conditioning index reads $1/\kappa = 99.321 \cdot 10^{-2}$, which is only slightly less than its optimal value of 1 for the isotropic pose.

In addition, due to the slightly misaligned manipulator configuration, the actual workspace shows a non-symmetrical shape with respect to both the base platform and tool platform reference system. Thus, Fig. 11 also depicts the tilt angle ϕ_t along the reachable workspace curve. One should note that the workspace depicted is based on the condition that $\phi_v = 0°$. Considering that the leg system is broadly of type SR—as observed from a simplified mechanics standpoint—the passive DOF around the axis between SPM-centre and foot-point may be exploited in regard of altering the workspace boundary curve that is depicted in Fig. 11. By this measure, the actual motion capability of the

Fig. 12 Example postures of the robot. Pictures A and B depict large values of h_t, while pictures C and D show small values of h_t. All four pictures show large tilt angle values α_t; however, A and C show negative ($\alpha_t < 0$), while B and D show positive values ($\alpha_t > 0$). In any case, the feet positions are identical in each posture, which allows the different postures of A and B or C and D to be functionally redundant
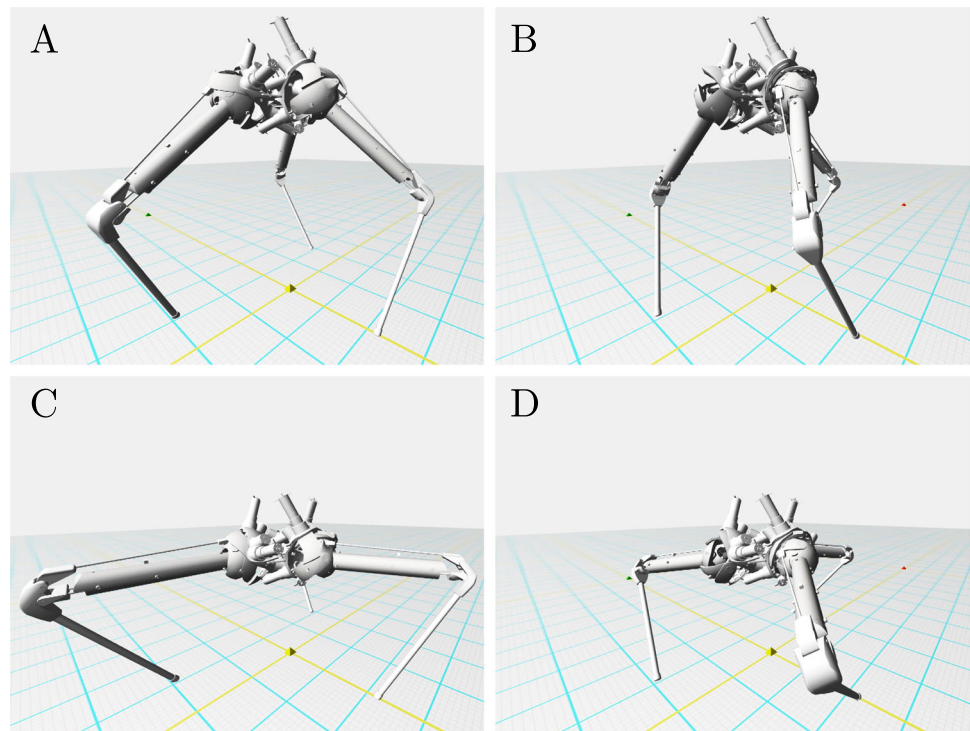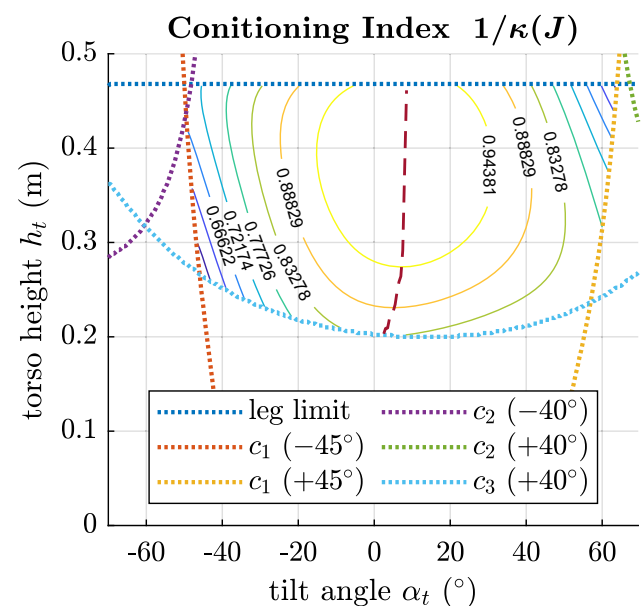

leg system may be enhanced in certain situations. This aspect is part of future research; however, the general capability for posture optimization is considered in the following analysis.

vidual target posture. A target is comprised of set values for the feet positions and the desired torso position and orientation. A video of the motion execution is included in the

3.4 Posture Dependent Conditioning

As one can observe from the Fig. 1, each leg features 4 DOFs, which results in a functional redundancy of the leg mechanism, as only 3 DOFs are required for the spatial positioning of the robot feet. This additional DOF is achieved by the tilt motion of the leg around the virtual axis between feet and hip centre. In the following, the possible existence of optimal postures for the maximization of the SPM conditioning index will be analyzed. This might be exploited as a kinematic optimization strategy to achieve better accuracy and a more balanced actuator torque distribution.

To analyze the optimality of the robot posture, a motion sequence characterized by two variable parameters—torso height h_t and leg tilt angle α_t—is established. For reference, in the undisturbed default robot pose with hip orientation ${}^*_{hb}\boldsymbol{R} \neq \boldsymbol{I}$, it holds $h_t = 0.38$ m and $\alpha_t = 0°$. At this angle, the leg is in the upright orientation, meaning that the plane defined by the direction vectors of the leg axes is vertical to the floor plane. Thus, the conditioning index $1/\kappa(\boldsymbol{J})$ is computed, while the height h_t of the torso centre and the leg angle α_t are varied between $h_t \in [0\,\mathrm{m}, 0.5\,\mathrm{m}]$ and $\alpha_t \in [-70°, +70°]$. Fundamentally, the experiment requires the full inverse kinematics solution for the complete robot model, which is implemented and computed for each indi-

Fig. 13 Conditioning index $1/\kappa(\boldsymbol{J})$ of the hip SPM depending on torso height h_t over floor level and redundant tilt angle α_t of the leg. Dotted lines depict different workspace limits due to joint ranges. The dashed line shows the path of best conditioning, depicting the ideal tilt angle α_t for each height h_t

supplementary materials. For reference, Fig. 12 depicts four extreme postures of the robot motion.

3.4.1 Results

The diagram in Fig. 13 shows kinematically feasible postures, framed by the mechanical limits of the joints, which are displayed by the dotted contours. Notably, the workspace is largely limited by the joint ranges of axes c_1, c_2 and c_3 of the support structure. In theory, c_1 does not strictly obey to a mechanical limit; however, due to electrical wiring and the increased possibility for internal mechanical collisions of the linkage structure itself, the axis c_1 was arbitrarily limited to an interval of $[+45°, -45°]$. The actual mechanical limits of the other axes c_2 and c_3 are fixed to $[+40°, -40°]$, which is in addition displayed in Table 2. Interestingly, the lower limit of axis c_3 is not reached in any posture due to constraints imposed by the leg parallel mechanism, which is bound to certain joint ranges itself. In any case, the region enclosed can be fully utilized for the optimization of the SPM conditioning index. In this regard, the red dashed line depicts the path of the most optimal posture over the variation of torso height h_t.

3.5 Robot Torso Workspace

The evaluation of the robot workspace is depicted in Fig. 14. In the initial posture, the torso centre is located at the origin with respect to the x- and y-axis of the world reference system. Identical to the previous analysis, the feet contact points are fixed and located symmetrically with a distance
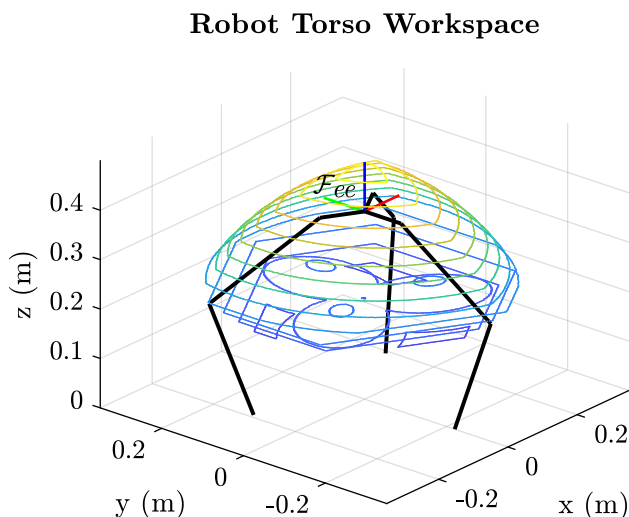
to the origin of $r_f = 0.22$ m. The figure shows the simplified geometric markup of the robot and its legs in the initial posture that is similar to the default one depicted in Fig. 1. Notably, no additional change of orientation was employed; hence Fig. 14 depicts only translational torso displacements. For reference, the vertical distance between each slice of the workspace depicted was selected with 2.5 cm. A planar projection is depicted in Fig. 15. In general, the workspace limit contours were evaluated via the observation of the allowed joint ranges, which must not be exceeded in order to avoid mechanical collisions between parts of the robot. However, the possible internal collision of neighbouring proximal and distal links of the hip SPMs was not included in this analysis, as this would require the implementation of complex intersection tests of the three-dimensional parts of the robot; yet, no critical geometrical intersection was observed visually during the analysis.

3.5.1 Results

As one can observe in the figure, the volume that depicts the robot workspace is essentially of ellipsoidal shape. In more detail, the horizontal layers of the workspace are shaped triangular with arched edges on the upper half, and shift to a hexagonal outer shape at the lower half. In addition, the workspace has spherically shaped cut-outs on the lower side, which is the result of the complicated joint range restrictions of each leg. However, the diagrams considering the condi-
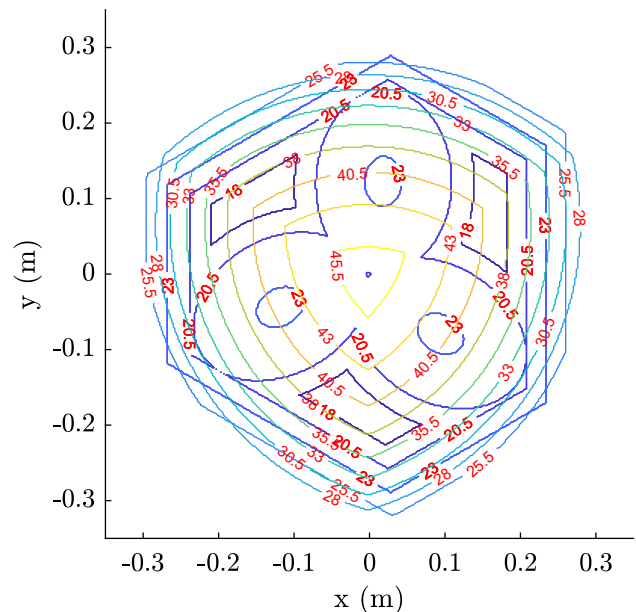

Robot Torso Workspace

Fig. 14 Workspace in the world reference system of the robot torso with feet positions fixed, which are located at $z = 0$ m and radius $r_f = 0.22$ m. The figure outlines the initial posture of the robot. $\mathcal{F}_{ee}$ depicts the torso centre reference frame, which defines the workspace after dislocation

Contours of Volume Slice Planes

Fig. 15 Contours of the robot workspace volume slice planes in the horizontal x-y-plane. The red annotations depict the slice hight levels in centimetres

tioning of the individual hip joints from Figs. 11 and 13 are still valid for the depicted workspace.

4 Performance Analysis

Beside expressing the configuration in terms of a single value $1/\kappa$ for accuracy, dexterity and distance to singularities, the implications on the torque requirements for the individual actuators is of practical interest. Due to the usage in a hip mechanism as part of a highly dynamic system, occurring external torques can vary highly in direction and amount, which requires sufficient torque capabilities of the actuators to cope with these demands. Since the maximum torque capability of the actuators is limited due to the lightweight overall robot design, which causes a trade-off between power and weight of the actuators, these limitations have to be considered as they may limit the performance of the robot at certain kinematic configurations. For reference, the employed actuators—considering motor and gear head—feature a maximum continuos torque of 1.6 Nm.

In the following, a Jacobian based performance measure is derived, evaluating the risk for overload situations of the actuators. For reference, many manipulator performance metrics and measures were proposed in the literature, as e.g. reviewed in [81, 82].

4.1 Critical Load Estimation

Supposing there exists an external load f defined in the hip base reference frame:

$$f = f_{max}\hat{f}, \tag{17}$$

with an arbitrary, yet normalized direction $\hat{f}$ and amount f_{max}, that is applied to the manipulator end-effector, then for the static case, the torque τ_j at the actuators $j = 1, 2, 3$ required to compensate this load can be calculated by:

$$\tau = J(\theta)^T f, \tag{18}$$

with $\tau = [\tau_1 \ \tau_2 \ \tau_3]^T$. Considering a worst case situation, an estimation of the necessary torques of the actuators for a given manipulator configuration is of interest. Since each row of J^T multiplied by the load torque vector f corresponds to an individual actuator torque τ_j, the maximum required actuator torque can be calculated by considering the 2-norm of the j-th row of J^T multiplied by the maximum external load $|f|$, yielding the inequality:

$$\tau_{j,max} = \left\| J_{j*}^T \right\| \cdot |f| \geq \left\| J_{j*}^T \cdot f \right\| = |\tau_j| \tag{19}$$

that is based on the submultiplicative property of the 2-norm. For the application, the relative notation is used, giving the worst case amplification of the external absolute end-effector torque in contrast to the demanded actuator torques:

$$\lambda_{j,rel} = \frac{\tau_{j,max}}{|f|} = \left\| J_{j*}^T \right\| = \left\| [J_{1k} \ J_{2k} \ J_{3k}] \right\|. \tag{20}$$

The elements of J are denoted for row j and column k by $J = (J_{jk})$. The maximum value is then considered as the critical design parameter:

$$\lambda_{max} = \max(\lambda_{1,rel}, \lambda_{2,rel}, \lambda_{3,rel}) \tag{21}$$

and is visualized in Fig. 16 for different configurations of the manipulator tool platform.

Apparently, with the matrix 2-norm being defined as $\|\cdot\| = \sigma_{max}(\cdot)$ [83, p. 128] with σ_{max} denoting the maximum singular value, yet the restriction to only single rows j of the Jacobian transpose J^T in Eq. 20, the calculation of λ_{max} becomes:

$$\lambda_{max} = \max_j \left(\sigma(J_{j*}^T) \right). \tag{22}$$

However, this yields a measure that is conceptually very similar to the minimum singular value (MSV) σ_{min} of the Jacobian matrix J. The MSV is a performance index [81] introduced in [84] and represents the maximum force transmission [85] of a manipulator configuration, which is defined as:

$$\sigma_{min} = \min_j(\sigma_j), \tag{23}$$

with σ_j being the singular values of the manipulator Jacobian matrix J. Notably, the MSV is a measure of the combined transmission ratio of all joint axes, while the index from Eq. 22 depicts each actuator axis separately. More specifically, the MSV σ_{min} expresses the maximum force transmission of the mechanism at its current configuration with bound joint torques $|\tau| = 1$. Consequently, this measure constitutes the combined work of all actuators to deliver the highest possible end effector torque $|f|$, without denoting any specific direction. Hence, one may express the relationship as:

$$\max_{|\tau|=1} |f| = \left\| (J^T)^{-1} \right\| \cdot |\tau| = \frac{1}{\sigma_{min}(J^T)} \cdot |\tau|. \tag{24}$$

On the contrary, the value from Eq. 22 depicts the maximum torque of each actuator that can be observed due to the application of the bound end effector force $|f| = 1$. Importantly, with Eq. 22 the direction of f is not specified and—in contrast to the MSV—may differ for each of the individual actuator torques. Thus, λ_{max} shows the maximum

force transmission for each joint axis, which is evaluated with $|\boldsymbol{f}| = f_{max} = 1$, yet independent directions $\hat{\boldsymbol{f}}$ for each actuator j and can be expressed by the relationship:

$$\max_{|\boldsymbol{f}|=1} |\tau_j| = \left\| \boldsymbol{J}_{j*}^T \right\| \cdot |\boldsymbol{f}| = \max_j \left(\sigma \left(\boldsymbol{J}_{j*}^T \right) \right) \cdot |\boldsymbol{f}|. \quad (25)$$

One should note that the conceptual basis of the approach taken considers each of the Jacobian transpose rows on its own, which is equivalent of observing the individual legs of a parallel manipulator. In this regard, a related idea based on screw theory was discussed in [86, 87], which describes the motion/force transmissibility of parallel manipulators. In [88] the application of the transmissibility index was performed for a spherical robot hand mechanism. Notably, due to its Jacobian based nature, the derived performance measure from Eq. 22 is related to the scaling factor from [89] that shows the maximum possible end-effector wrench for a given direction within the actuator limits. Similarly, the measure is related to the payload capability index [90, 91] that determines weather a manipulator is able to withstand a force applied to the end-effector.

Finally, Fig. 16 serves as an estimation of the worst case situation that a single actuator of the hip unit may encounter; thus, it is expressed with regard to the orientation of the base platform reference system in the robot assembly. This means that any orientation of the manipulator depicted in the figure is expressed via Eq. 3 with the home configuration ${}_{hb}^{hf}\boldsymbol{R} = {}_{hb}^{*}\boldsymbol{R} \neq \boldsymbol{I}$ for the values $\phi_v = 0$, $\phi_t = 0$ and $\phi_r = 0$.

Consequently, Fig. 16 shows both the critical torque and the dexterity index for different initial twists, while tilting the manipulator by ϕ_t. Thus, Fig. 16 basically projects the spatial depiction of Fig. 9 onto a polar-surface representation. In this regard, in the default posture at $\phi_v = 0$, $\phi_t = 0$ and $\phi_r = 0$, the ${}^{hf}\hat{\boldsymbol{e}}_x$-axis points at the polar angle 0° and the ${}^{hf}\hat{\boldsymbol{e}}_y$-axis at the polar angle 90°, while the ${}^{hf}\hat{\boldsymbol{e}}_z$-axis is aligned vertically to the paper plane in the centre point. Thus, the actuator at $\hat{\boldsymbol{u}}_1$ is located at the polar angle 0° due to projection. Noticeably, the inclusion of the misaligned orientation ${}_{hb}^{*}\boldsymbol{R}_i$ of the SPM in the default posture yields the asymmetrical results that are depicted in the figure.

One important note to make here is the commitment towards the *right-branch*-configuration as it is called by the author of this paper, which expresses the general direction of the proximal link, if viewed along the base vector $\hat{\boldsymbol{u}}_j$ to the SPM centre. The mirrored *left-branch*-configuration has no disadvantage, but is not considered in the data depicted in the figures.

4.1.1 Results

As can be seen in Fig. 16, the actuator load varies significantly in dependence to the manipulator twist ϕ_v, which

Torque and Dexterity over Workspace
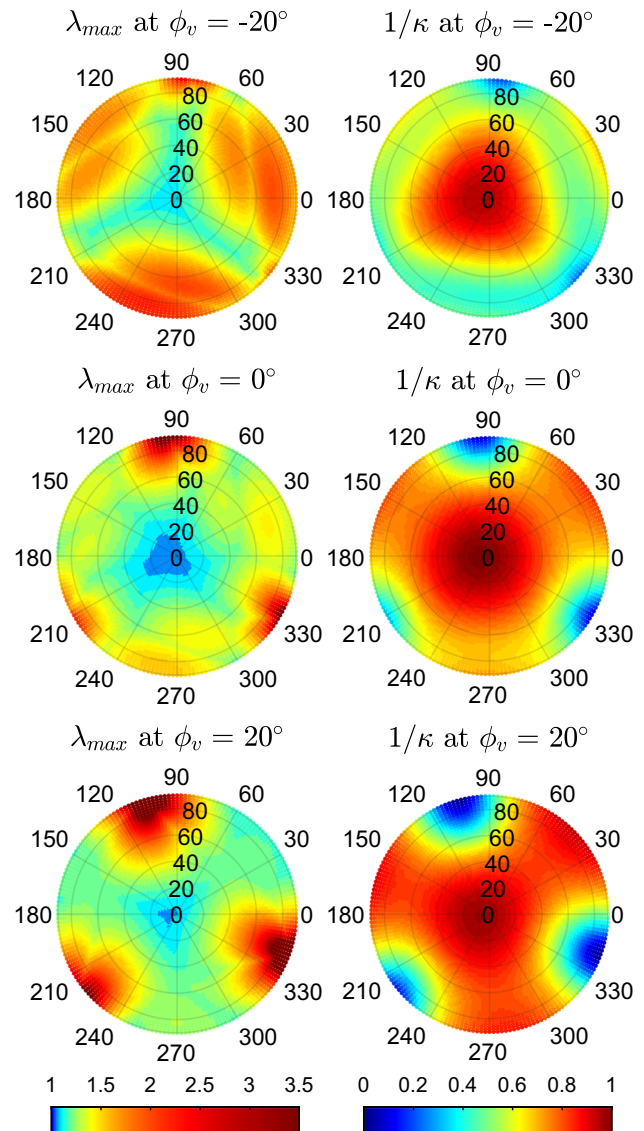
Fig. 16 Maximum worst-case amplification λ_{max} of the actuators and corresponding dexterity index $1/\kappa$ for different twists ϕ_v of the end-effector. Values along the radius depict the tilt angle ϕ_t. The function for the nonlinear scaling of the color map for the left side plots reads $f(x) = 100^{x-0.799} + 0.975$

becomes increasingly problematic at higher tilting angles ϕ_t of the tool platform. However, the figure shows that there exist regions in which the accuracy of the manipulator is still sufficient, but the worst case load amplification on the actuators becomes unmanageable large. This must be considered with caution as a measure to prevent individual actuators from overload situations. Notably, due to visualization purposes and the depiction of a reasonable range, the maximum load amplification is capped at a maximum value of 3.5 in the figure, which in reality increases exponentially close to the regions of singularities. Considering that the manipulator is

indented to perform motion and locomotion tasks that eventually require to cope with high impacts and large torques, the accuracy that is achieved in these situations is considered to be of lesser importance. In addition, due to the support structure that restricts the workspace of the hip manipulator to fixed maximum tilt angles, it is not possible for the SPM in this robot to come close to postures with either very low dexterity values or unreasonably high critical load values for individual actuators. The variability between the critical load amplification λ_{max} and the dexterity $1/\kappa$ is expressed in Fig. 17 that shows the corresponding curvatures at the default twist angle $\phi_v = 0°$ over the full rotational range $\phi_r \in [-\pi, +\pi]$ for different tilt angles ϕ_t. However, according to Fig. 16, problematic configurations may be reached at tilt angles of more than 60°, which is mechanically not possible with the current robot model.

5 Discussion

Regarding the overall concept of the robot, several points of interest must be discussed, considering the significance of the proposed design stemming from the combination of the fundamental design methods (I–V) and their mechanical realization from Sec. 2 with respect to the results from Secs. 3 and 4.

5.1 Dexterity Considerations

Fundamentally, due to the design of the robot requiring a dense interlocking assembly of the hip units, a general asymmetrical mechanical layout is the result. Consequently, this dictates the specific orientation of the hip base and tool platforms in the default robot posture.

Load Ampl. to Dex. Curvature at $\phi_v = 0°$
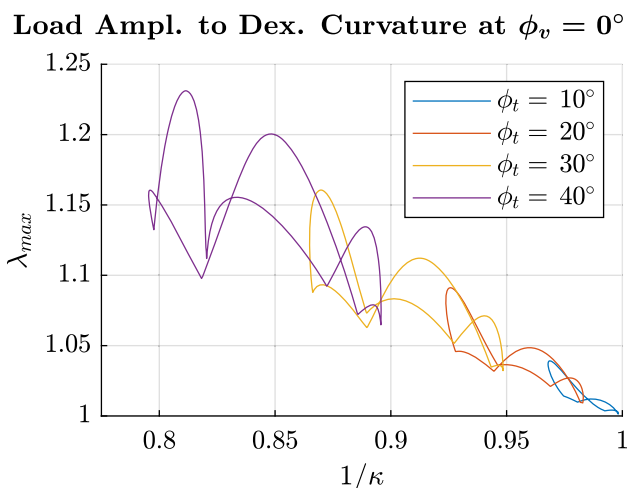
Fig. 17 Curvatures, depicting the relationship between load amplification λ_{max} and dexterity $1/\kappa$ for $\phi_v = 0°$ over $\phi_r \in [-\pi, +\pi]$

Still, it was possible to find an orientation avoiding mechanical collisions of the platforms that enables a natural and stable tripodal pose in a nearly isotropic configuration. This can be deduced from the results of Sec. 3.3, which show a promising characteristic of the SPM regarding its utilization as a hip joint in the legged robot. Specifically, the results reveal that the condition of the SPM stays at a configuration balanced reasonably well over its entire workspace.

As a remark, evaluating the global performance of the robot concerning accuracy, dexterity and actuator load amplification may require a different approach, as the analysis of the properties regarding the whole robot model involves the inclusion of all 12 DC-motors. Thus, the global accuracy of the robot may be limited to a certain degree based on the posture and kinematic properties of the leg closed-loop structure related to the knee motion, which must be evaluated in future works. Fundamentally, to evaluate the overall performance of the robot in its tripodal posture, it must be considered how the joint errors will be amplified through the system towards the torso end-effector, which thus results in a combination of both rotational and translational motion. However, this yields a Jacobian matrix with heterogeneous units; thus, the application of the condition number is considered problematic [34, p.166]. Furthermore, as a consequence of the functional redundancy of the robot 4-DOF leg design, the robot instantaneous velocity mapping is represented by a Jacobian of non-square dimension. Still, joint error propagation may become an important consideration when transitioning to a real world system, as manufacturing inaccuracies, material imperfections and model parameter uncertainties will influence the systemic behaviour to some degree.

However, a small overall workspace of the hip units as a result of mechanical limitations imposed by the central support structure might limit the range of motion to a degree that this possibly prevents the robot from adopting certain postures; yet this might be improved by a future redesign regarding the geometry of involved mechanical parts. Notably, the linkage structure itself uses complex three-dimensional shapes, which makes it difficult to strictly prevent collisions at larger motions of the tool platform. However, with the workspace limited by the universal joint, this prevents the SPM linkage structure to enter postures that are mechanically not feasible or could potentially damage the mechanism.

A crucial aspect that directly stems from the design of the robot topology considers the placement of the knee actuator itself as a part fixed to the universal joint structure. Consequently, this allows for a free rotation of the knee actuator around the DOF of axis c_1 inside the robot torso. By this measure, torque exerted by this actuator cannot contradict the motion of the tool platform, as the actuator is technically part of the upper leg due to its series placement with respect to the hip mechanism. Thus, the series–parallel layout inherently allows for the knee actuator to work independently of

the hip actuators, as it must not actively compensate for any motion of the tool platform, which would be the case if the actuator had been fixed to the torso. As a result, which is important regarding any manipulation tasks, the knee actuation therefore does not influence the conditioning of the hip mechanisms that was revealed by Sec. 3.3.

Furthermore, the results from Sec. 3.4 reveal that the additional DOF of the leg construction offers the possibility to further exploit the functional redundancy of the mechanism, which benefits dexterity and load distribution. Crucially, the 4-DOF layout of the robot legs specifically allows for the optimization of the hip mechanism conditioning index for different target postures via small tilt motions of the leg. Consequently, this can increase the overall accuracy of the robot regarding manipulation tasks and can situational lower the individual torque requirements for the actuators.

5.2 Workspace Considerations

As noted in the analysis of the robot workspace in Sec. 3.5, using the torso as a general end-effector, only translational motion was considered. Thus, it might be possible to increase the reachable workspace via the optimization of torso orientation and improved feet placement. Still, without additional optimizations, the analysis shows that the resulting workspace is large enough to allow for general manipulation tasks.

Notably, the specific mechanical realization of the leg compliance possess practical implications on the applicability of the robot regarding manipulation tasks and locomotion. Specifically, by altering the spring stiffness and pre-stressed state of the internal leg spring, the leg behaviour can be adjusted for either no compliance, full compliance or a mixture of both.

In this regard, the specific behaviour of the series elasticity contained in the robot legs allows that slow motion may be performed in a stiff and statically stable pose, while fast motion translates into a compliant reaction of the legs. This is important, as the workspace revealed in Sec. 3.5 can only be utilized for accurate manipulations tasks if the robot obeys to a stiff configuration.

Consequently, the robot may be suitable for both accurate object manipulation and agile legged locomotion, which is a combination with interesting potential.

5.3 Performance Considerations

As examined in Sec. 4.1, one important aspect that was encountered as a consequence of the specific parallel mechanism concerns the required actuator torques that will rise under large deviations from the manipulator isotropic pose.

As revealed by the results, the worst-case load amplification stays at a small number, which is crucial to the feasibility

of the robot for the desired task of legged locomotion. Fundamentally, exceeding the physical performance limitations of a single actuator may result in the loss of general controllability. In certain conditions, this might yield the robot to lose stability and may potentially result in the robot collapsing. However, as the results show, regarding the intended workspace of the manipulator, both the actual dexterity and the actuator load amplification torques do not reach values that might be considered as critical. Thus, the final configuration shows great potential for proving itself sufficient for the task of legged locomotion. Notably, if future work will investigate possible improvements to the limited workspace of the SPM, this might allow the system to enter less well conditioned postures.

In this regard, a design component directly connected to the applicability of the analysis is the non-overconstrained general mechanical realization of the hip joints. Due to the functional separation of hip torques and forces, as realized through the integration of the hip universal joint, the properties of parallel mechanisms can be exploited while relying on the structural stiffness of the internal joint. This functional separation solves the problem of overly stressed linkages, which might bent otherwise and allows for a generally more compact robot. Hence, the linkage rigidity must only compensate for the transmitted torque, which consequently can be physically considered by observing the worst-case load amplification indicator from Sec. 4.1.

6 Conclusion

In this article, the concept and design for a novel three-legged robot was presented. The robot involves a serial-parallel actuation layout, leg compliance, a functional separation of impact forces and actuation torques, a close interlocking arrangement of the actuators, a dense mass concentration and a lightweight, interconnected mechanical design.

Crucially, the integration of the parallel hip actuation equips the robot with the theoretical capability for precise and fast motion, which in combination with the three-legged layout, gives the robot the option to perform accurate manipulation tasks in a statically stable pose. Furthermore, the analysis of the hip mechanism revealed a restricted, yet reasonable sufficient workspace for the robot torso motion. In addition, the analysis showed that the posture of the hip mechanism was always well-conditioned as the manipulator is mechanically limited to enter critical regions. In this regard, the robot allows for kinematic optimizations due its functionally redundant 4-DOF leg design. Noticeably, due to the utilization of the serial-parallel layout the conditioning of the hip manipulators was not affected by the knee actuation. Additionally, the internal support structure relieves the linkages themselves from coping with additional forces.

Combined with the dense mass concentration in the robot torso and its lightweight and agile, yet compliant legs, the robot may be highly suitable for dynamically balanced locomotion, as the overall robot design conceptually resembles the SLIP model. Finally, a performance index was derived for the evaluation of overload situations of individual actuators, which—due to the current workspace—revealed that the actuators are not prone to experience critical states.

7 Future Work

The main objective—considering future work—of the proposed robot can be divided into the capability to perform legged locomotion and manipulation tasks using its torso as a general end-effector.

Regarding manipulation tasks in its tripodal standing posture, possible control strategies may involve the application of simple task space PID control schemes for the motion of the robot torso. This might be sufficient regarding the condensed mass distribution of the mechanical system, possibly allowing for these more kinematically driven control approaches to work.

However, considering legged locomotion, the overall complexity required from the controller design to cope with the inherently fragile stability of the robot—based on its untypical three-legged design—naturally requires some form of dynamically stable balancing due to the underactuated systemic state if one or more legs are not in contact with the ground surface. Notably, as a mechanical solution, symmetrically extending the number of legs connected to the robot torso obviously lowers the complexity of the required control task, as increasing the number of legs will allow for a wider range of statically stable postures and more varied gaits. However, this would compromise the concept of an agile and lightweight design and requires to alter the orientation of the hip manipulators, possibly degrading the general closeness to the ideal isotropic posture.

Consequently, dynamic locomotion requires more sophisticated approaches of the controller design. Possible research might investigate existing SLIP control schemes due to the similarity of the overall robot topology to this fundamental model. This extends for example to the application of robust nonlinear model predictive control, as the complexity and posture redundancy of the system might benefit from these approaches. To some extend, the design of the robot may generally allow for the effective application of model-based control solutions, possibly based on the reliance on a reduced order dynamics representation of the robot that still closely resembles the real system. Alternatively, model-free reinforcement learning algorithms might yield feasible motion policies.

In this regard, future work will explore both the implementation of control strategies in simulation and real-time hardware, as well as the transition from simulations of the robot to actual real world performances.

Supplementary Material

The following supplementary materials are included with this article. Alternatively, the contents can be found at the authors Github website [92]:

- Video of the motion sequence of the robot performed for the posture depended conditioning analysis from Sec. 3.4: File `PostureDependentConditioning.mp4`.
- Several data tables, numerically depicting the data that is represented in the following figures: Figs. 9, 10, 11, 13, 14, 15, 16 and 17.

Declarations

References

1. Blickhan, R.: The spring-mass model for running and hopping. J. Biomech. **22**(11), 1217–1227 (1989). https://doi.org/10.1016/0021-9290(89)90224-8. (http://www.sciencedirect.com/science/article/pii/0021929089902248)

2. Feller, D., Siemers, C.: Topological analysis of a novel compact omnidirectional three-legged robot with parallel hip structures regarding locomotion capability and load distribution. Robotics **10**(4), (2021). https://doi.org/10.3390/robotics10040117. https://www.mdpi.com/2218-6581/10/4/117

3. Feller, D., Siemers, C.: Mechanical design and analysis of a novel three-legged, compact, lightweight, omnidirectional, serial–parallel robot with compliant agile legs. Robotics **11**(2), (2022). https://doi.org/10.3390/robotics11020039. https://www.mdpi.com/2218-6581/11/2/39

4. He, J., Gao, F.: Mechanism, actuation, perception, and control of highly dynamic multilegged robots: A review. Chin J Mech Eng **33** (2020). https://doi.org/10.1186/s10033-020-00485-9

5. Chen, Z., Gao, F.: Time-optimal trajectory planning method for six-legged robots under actuator constraints. Proc. Inst. Mech. Eng. C J. Mech. Eng. Sci. **233**, 095440621983307 (2019). https://doi.org/10.1177/0954406219833077

6. Vukobratovic, M., Borovac, B.: Zero-moment point - thirty five years of its life. I. J. Humanoid Robotics **1**, 157–173 (2004). https://doi.org/10.1142/S0219843604000083

7. Grimes, J., Hurst, J.: The design of atrias 1.0: a unique monopod, hopping robot. Proceedings of the 15th International Conference on Climbing and Walking Robots and the Support Technologies for Mobile Machines (CLAWAR), Baltimore, MD 548–554 (2012). https://doi.org/10.1142/9789814415958_0071

8. Gong, Y., et al.: Feedback control of a cassie bipedal robot: Walking, standing, and riding a segway. 2019 American Control Conference (ACC) 4559–4566 (2019). https://doi.org/10.23919/ACC.2019.8814833

9. Raibert, M.H., H. Benjamin Brown, J., Chepponis, M.: Experiments in balance with a 3d one-legged hopping machine. The Int. J. Robot. Res. **3**(2), 75–92 (1984). https://doi.org/10.1177/027836498400300207

10. Yim, J.K., Wang, E.K., Fearing, R.S.: Drift-free roll and pitch estimation for high-acceleration hopping. In: 2019 International Conference on Robotics and Automation (ICRA), pp. 8986–8992 (2019). https://doi.org/10.1109/ICRA.2019.8793259

11. Ren, P., Hong, D.: Triple Stance Phase Displacement Analysis With Redundant and Nonredundant Sensing in a Novel Three-Legged Mobile Robot Using Parallel Kinematics. J Mech Robot **1**(4), (2009). https://doi.org/10.1115/1.3204251. https://arxiv.org/abs/https://asmedigitalcollection.asme.org/mechanismsrobotics/article-pdf/1/4/041001/5931641/041001_1.pdf

12. Oki, K., Ishikawa, M., Li, Y., Yasutani, N., Osuka, K.: Tripedal walking robot with fixed coxa driven by radially stretchable legs. In: 2015 IEEE/RSJ International Conference on Intelligent Robots and Systems (IROS), pp. 5162–5167 (2015). https://doi.org/10.1109/IROS.2015.7354104

13. Li, K., et al.: Predictive control of stable standing of three-legged robot. In: 2019 Chinese Automation Congress (CAC), pp. 2797–2802 (2019). https://doi.org/10.1109/CAC48633.2019.8997353

14. Cui, H., et al.: A new design of three-legged robot of mechanical and control system. Appl Mech Mater 347–350 (2013). https://doi.org/10.2991/isccca.2013.126

15. Masuda, Y., Ishikawa, M.: Simplified triped robot for analysis of three-dimensional gait generation. Journal of Robotics and Mechatronics **29**(3), 528–535 (2017). https://doi.org/10.20965/jrm.2017.p0528

16. dos Santos, J.L., Nascimento, C.L.: Gait synthesis for a three-legged robot using learning automata. In: 2011 15th International Conference on Advanced Robotics (ICAR), pp. 271–276 (2011). https://doi.org/10.1109/ICAR.2011.6088586

17. Rosyid, A., Stefanini, C., El-Khasawneh, B.: A reconfigurable parallel robot for on-structure machining of large structures. Robotics **11**(5), (2022). https://doi.org/10.3390/robotics11050110. https://www.mdpi.com/2218-6581/11/5/110

18. Marm, the new three-leg robot to transport weights and manipulate components in space (2022). https://opentalk.iit.it/en/marm-the-new-three-leg-robot-to-transport-weights-and-manipulate-components-in-space/. Accessed 20 May 2023

19. Baumgärtner, J., et al.: Triped, non-mimetic walking system for research on novel locomotion methods (2022). https://triped-robot.github.io/. https://www.imt.uni-stuttgart.de/en/research/research-projects/triped/. Accessed 20 May 2023

20. Hutter, M., et al.: ANYmal - a highly mobile and dynamic quadrupedal robot. In: 2016 IEEE/RSJ International Conference on Intelligent Robots and Systems (IROS), pp. 38–44 (2016). https://doi.org/10.1109/IROS.2016.7758092

21. Bledt, G., et al.: MIT Cheetah 3: design and control of a robust, dynamic quadruped robot. In: 2018 IEEE/RSJ International Conference on Intelligent Robots and Systems (IROS), pp. 2245–2252 (2018). https://doi.org/10.1109/IROS.2018.8593885

22. Park, H.-W., Wensing, P.M., Kim, S.: High-speed bounding with the mit cheetah 2: Control design and experiments. The Int. J. Robot. Res. **36**(2), 167–192 (2017). https://doi.org/10.1177/0278364917694244

23. Ceccarelli, M., Cafolla, D., Russo, M., Carbone, G.: Heritagebot platform for service in cultural heritage frames. Int. J. Adv. Robot. Syst. **15**(4), 1729881418790692 (2018). https://doi.org/10.1177/1729881418790692

24. Sun, Q., Chen, X.: Towards dynamic alternating tripod trotting of a pony-sized hexapod robot for disaster rescuing based on multi-modal impedance control. Robotica **36**, 1–29 (2018). https://doi.org/10.1017/S026357471800022X

25. Kenneally, G., De, A., Koditschek, D.E.: Design principles for a family of direct-drive legged robots. IEEE Robotics and Automation Letters **1**(2), 900–907 (2016). https://doi.org/10.1109/LRA.2016.2528294

26. Zhao, Y., Gao, F., Zhao, Y., Chen, Z.: Peg-in-hole assembly based on six-legged robots with visual detecting and force sensing. Sensors **20**(10), (2020). https://doi.org/10.3390/s20102861. https://www.mdpi.com/1424-8220/20/10/2861

27. Arm, P., et al.: SpaceBok: a dynamic legged robot for space exploration. In: 2019 International Conference on Robotics and Automation (ICRA), pp. 6288–6294 (2019). https://doi.org/10.1109/ICRA.2019.8794136

28. Kang, R., et al.: Structural design and crawling pattern generator of a planar quadruped robot for high-payload locomotion. Sensors **20**(22), (2020). https://doi.org/10.3390/s20226543. https://www.mdpi.com/1424-8220/20/22/6543

29. Pan, Y., Gao, F.: A new six-parallel-legged walking robot for drilling holes on the fuselage. Proc. Inst. Mech. Eng. C J. Mech. Eng. Sci. **228**(4), 753–764 (2014). https://doi.org/10.1177/0954406213489068

30. Zhong, G., Deng, H., Xin, G., Wang, H.: Dynamic hybrid control of a hexapod walking robot: Experimental verification. IEEE Trans. Ind. Electron. **63**(8), 5001–5011 (2016). https://doi.org/10.1109/TIE.2016.2551679

31. Yang, P., Gao, F.: eg kinematic analysis and prototype experiments of walking-operating multifunctional hexapod robot. Proc Inst. Mech. Eng. C J. Mech. Eng. Sci. **228**(12), 2217–2232 (2014). https://doi.org/10.1177/0954406213516087

32. Jia, S., Chen, W., Zhang, W., Wu, H., Li, W.: Kinematics analysis of walking robot based on double stewart parallel mechanism 5530–5535 (2019). https://doi.org/10.1109/CAC48633.2019.8996334

33. Liu, J., Chen, Z., Gao, F.: Kinematic calibration of a six-legged walking machine tool **35** (2022). https://doi.org/10.1186/s10033-022-00688-2

34. Merlet, J.: Parallel Robots Solid Mechanics and Its Applications. Springer, Netherlands (2005)

35. Russo, M., Cafolla, D., Ceccarelli, M.: Design and experiments of a novel humanoid robot with parallel architectures. Robotics **7**(4), (2018). https://doi.org/10.3390/robotics7040079. https://www.mdpi.com/2218-6581/7/4/79

36. Russo, M., Ceccarelli, M.: Kinematic design of a tripod parallel mechanism for robotic legs. 121–130 (2018). https://doi.org/10.1007/978-3-319-60702-3_13

37. Camacho-Arreguin, J.I., Wang, M., Russo, M., Dong, X., Axinte, D.: Novel reconfigurable walking machine tool enables symmetric and nonsymmetric walking configurations. IEEE/ASME Transactions on Mechatronics 1–12 (2022). https://doi.org/10.1109/TMECH.2022.3183689

38. Li, L., Fang, Y., Guo, S., Qu, H., Wang, L.: Type synthesis of a class of novel 3-dof single-loop parallel leg mechanisms for walking robots. Mech. Mach. Theory **145**, 103695 (2020). https://doi.org/10.1016/j.mechmachtheory.2019.103695. https://www.sciencedirect.com/science/article/pii/S0094114X19323018

39. Figliolini, G., Rea, P., Conte, M.: Mechanical design of a novel biped climbing and walking robot. In: Parenti Castelli, V., Schiehlen, W. (eds.) ROMANSY 18 Robot Design, Dynamics and Control, pp. 199–206. Springer Vienna, Vienna (2010)

40. Jian-she, G., Ming-xiang, L., Yu-Yin, L., Bao-tang, W.: Singularity analysis and dimensional optimization on a novel serial-parallel leg mechanism. Procedia Engineering **174**, 45–52 (2017). https://doi.org/10.1016/j.proeng.2017.01.140. https://www.sciencedirect.com/science/article/pii/S1877705817301406, 13th Global Congress on Manufacturing and Management Zhengzhou, China 28-30 November, 2016

41. Zhao, J., Liu, K., Zhao, F., Sun, Z.: Design and kinematic analysis on a novel serial-parallel hybrid leg for quadruped robot. In: Yu, H., et al. (eds.) Intelligent Robotics and Applications, pp. 436–447. Springer International Publishing, Cham (2019)

42. Zhang, Z., Meng, G.: Design and analysis of a six degrees of freedom serial-parallel robotic mechanism with multi-degree of freedom legs. Int. J. Adv. Robot. Syst. **15**(6), 1729881418812643 (2018). https://doi.org/10.1177/1729881418812643

43. Reinaldo, C., Phu, S.N., Essomba, T., Nurahmi, L.: Kinematic comparisons of hybrid mechanisms for bone surgery: 3-prp-3-rps and 3-rps-3-prp. Machines **10**(11), (2022). https://doi.org/10.3390/machines10110979. https://www.mdpi.com/2075-1702/10/11/979

44. Gosselin, C., Angeles, J.: The Optimum Kinematic Design of a Spherical Three-Degree-of-Freedom Parallel Manipulator. J. Mech. Transm. Autom. Des. **111**(2), 202–207 (1989). https://doi.org/10.1115/1.3258984. (https://arxiv.org/abs/https://asmedigitalcollection.asme.org/mechanicaldesign/article-pdf/111/2/202/5817629/2021.pdf)

45. Altan, A., Hacıoğlu, R.: Model predictive control of three-axis gimbal system mounted on uav for real-time target tracking under external disturbances. Mech. Syst. Signal. Process. **138**, 106548 (2020). https://doi.org/10.1016/j.ymssp.2019.106548. https://www.sciencedirect.com/science/article/pii/S0888327019307691

46. Gosselin, C., Angeles, J.: A Global Performance Index for the Kinematic Optimization of Robotic Manipulators. J. Mech. Des. **113**(3), 220–226 (1991). https://doi.org/10.1115/1.2912772. (https://arxiv.org/abs/https://asmedigitalcollection.asme.org/mechanicaldesign/article-pdf/113/3/220/5796880/2201.pdf)

47. Gosselin, C.M., Lavoie, E.: On the kinematic design of spherical three-degree-of-freedom parallel manipulators. The Int. J. Robot. Res. **12**(4), 394–402 (1993). https://doi.org/10.1177/027836499301200406

48. Gosselin, C.M., Hamel, J.: The agile eye: a high-performance three-degree-of-freedom camera-orienting device (1994)

49. Gosselin, C.M.: Simulation and computer-aided kinematic design of three-degree-of-freedom spherical parallel manipulators. J. Robot. Syst. **12**(12), 857–869 (1995). https://doi.org/10.1002/rob.4620121209

50. Gosselin, C.M., Gagné, M.: A closed-form solution for the direct kinematics of a special class of spherical three-degree-of-freedom parallel manipulators. In: Merlet, J.-P., Ravani, B. (eds.) Computational Kinematics '95, pp. 231–240. Springer, Netherlands, Dordrecht (1995)

51. Gosselin, C.M., St Pierre, E., Gagne, M.: On the development of the agile eye. IEEE Robot. Autom. Mag. **3**(4), 29–37 (1996)

52. Huang, Z., Yao, Y.L.: A new closed-form kinematics of the generalized 3-dof spherical parallel manipulator. Robotica **17**(5), 475–485 (1999). https://doi.org/10.1017/S0263574799001630

53. Bonev, I., Chablat, D., Wenger, P.: Working and assembly modes of the agile eye. In: Proceedings 2006 IEEE International Conference on Robotics and Automation, 2006. ICRA 2006, pp. 2317–2322 (2006). https://doi.org/10.1109/ROBOT.2006.1642048

54. Bai, S., Hansen, M.R., Angeles, J.: A robust forward-displacement analysis of spherical parallel robots. Mech. Mach. Theory **44**(12), 2204–2216 (2009). https://doi.org/10.1016/j.mechmachtheory.2009.07.005. (https://www.sciencedirect.com/science/article/pii/S0094114X09001347)

55. Al-Widyan, K., Ma, X.Q., Angeles, J.: The robust design of parallel spherical robots. Mech. Mach. Theory **46**(3), 335–343 (2011). https://doi.org/10.1016/j.mechmachtheory.2010.11.002. (https://www.sciencedirect.com/science/article/pii/S0094114X10001928)

56. Wu, G., Bai, S., Kepler, J.: Mobile platform center shift in spherical parallel manipulators with flexible limbs. Mech. Mach. Theory **75**, 12–26 (2014). https://doi.org/10.1016/j.mechmachtheory.2014.01.001

57. Chaker, A., Mlika, A., Laribi, m.a., Romdhane, L., Zeghloul, S.: Synthesis of spherical parallel manipulator for dexterous medical task. Frontiers of Mechanical Engineering **7** (2012). https://doi.org/10.1007/s11465-012-0325-4

58. Saafi, H., Laribi, M.A., Zeghloul, S.: Resolution of spherical parallel manipulator (spm) forward kinematic model (fkm) near the singularity (2013)

59. Saafi, H., Laribi, M.A., Zeghloul, S.: Forward kinematic model improvement of a spherical parallel manipulator using an extra sensor. Mech. Mach. Theory **91**, 102–119 (2015). https://doi.org/10.1016/j.mechmachtheory.2015.04.006. (https://www.sciencedirect.com/science/article/pii/S0094114X15000798)

60. Saafi, H., Vulliez, M., Zeghloul, S., Laribi, M.A.: A new serial approach of the forward kinematic model of spherical parallel manipulators for real-time applications. Proc. Inst. Mech. Eng. C J. Mech. Eng. Sci. **232**(4), 677–684 (2018). https://doi.org/10.1177/0954406216688027

61. Houssem, S., Laribi, m.a., Zeghloul, S.: Forward kinematic model resolution of a special spherical parallel manipulator: Comparison and real-time validation. Robotics **9**, 62 (2020). https://doi.org/10.3390/robotics9030062

62. Essomba, T., et al.: Torque reduction of a reconfigurable spherical parallel mechanism based on craniotomy experimental data. Appl. Sci. **11**(14) (2021). https://www.mdpi.com/2076-3417/11/14/6534. https://doi.org/10.3390/app11146534

63. Zhang, J., et al.: Module combination based configuration synthesis and kinematic analysis of generalized spherical parallel mechanism for ankle rehabilitation. Mech. Mach.

Theory **166**, 104436 (2021). https://www.sciencedirect.com/science/article/pii/S0094114X21001944. https://doi.org/10.1016/j.mechmachtheory.2021.104436

64. Zou, Y., et al.: Design and experimental research of 3-rrs parallel ankle rehabilitation robot. Micromachines **13**(6) (2022). https://www.mdpi.com/2072-666X/13/6/950. https://doi.org/10.3390/mi13060950

65. Du, Y., Li, R., Li, D., Bai, S.: An ankle rehabilitation robot based on 3-rrs spherical parallel mechanism. Advances in Mechanical Engineering **9**, 168781401771811 (2017). https://doi.org/10.1177/1687814017718112

66. Sadeqi, S., Bourgeois, S.P., Park, E.J., Arzanpour, S.: Design and performance analysis of a 3-rrr spherical parallel manipulator for hip exoskeleton applications. Journal of Rehabilitation and Assistive Technologies Engineering **4**, 2055668317697596 (2017). https://doi.org/10.1177/2055668317697596, pMID: 31186926

67. Lee, J., Kim, H., Yang, W.: Development of wrist interface based on fully actuated coaxial spherical parallel mechanism for force interaction. Sensors **21**(23) (2021). https://www.mdpi.com/1424-8220/21/23/8073. https://doi.org/10.3390/s21238073

68. Leal-Naranjo, J., Wang, M., Paredes Rojas, J.C., Rostro-Gonzalez, H.: Design and kinematic analysis of a new 3-dof spherical parallel manipulator for a prosthetic wrist. J. Braz. Soc. Mech. Sci. **42** (2019). https://doi.org/10.1007/s40430-019-2153-5

69. Chen, Y.J., et al.: Designing and controlling a self-balancing platform mechanism based on 3-RCC spherical parallel manipulator. Robotic Systems and Applications (2023). https://doi.org/10.21595/rsa.2023.23015

70. Hofschulte, J.: Zweibeiniger Roboter mit parallelkinematischen Hüftgelenken. Books on Demand GmbH, Norderstedt (2006)

71. Hofschulte, J., Seebode, M., Gerth, W.: Parallel manipulator hip joint for a bipedal robot. Climbing and Walking Robots, pp. 601–60. Springer Berlin Heidelberg, Berlin, Heidelberg (2005)

72. Gao, J.-S., Wang, Y.-C., Liu, D.-P., Zuo, W.-L.: Simulation and experiment on the serial-parallel leg of a novel quadruped walking robot. In: 2016 IEEE International Conference on Mechatronics and Automation, pp. 165–170 (2016). https://doi.org/10.1109/ICMA.2016.7558554

73. Geyer, H., Saranli, U.: Gait based on the spring-loaded inverted pendulum. Humanoid Robotics: A Reference (2017). https://doi.org/10.1007/978-94-007-7194-9_43-1

74. Pratt, J., Chew, C.-M., Torres, A., Dilworth, P., Pratt, G.: Virtual model control: An intuitive approach for bipedal locomotion. The Int. J. Robot. Res. **20**(2), 129–143 (2001). https://doi.org/10.1177/02783640122067309

75. Rad, H., Gregorio, P., Buehler, M.: Design, modeling and control of a hopping robot. **3**, 1778–1785 (1993). https://doi.org/10.1109/IROS.1993.583877

76. Bonev, I.A.: Geometric analysis of parallel mechanisms (2002). https://www.etsmtl.ca/Professeurs/ibonev/documents/pdf/ThesisBonev.pdf

77. Bonev, I.A.: Direct kinematics of zero-torsion parallel mechanisms. In: 2008 IEEE International Conference on Robotics and Automation, pp. 3851–3856 (2008). https://doi.org/10.1109/ROBOT.2008.4543802

78. Bonev, I., Ryu, J.: Orientation workspace analysis of 6-dof parallel manipulators (1999). https://doi.org/10.1115/DETC99/DAC-8646

79. Craig, J.J.: Introduction to Robotics: Mechanics and Control 3rd edn. Pearson (2003)

80. Salisbury, J.K., Craig, J.J.: Articulated hands: Force control and kinematic issues. The Int. J. Robot. Res. **1**(1), 4–17 (1982). https://doi.org/10.1177/027836498200100102

81. Patel, S., Sobh, T.: Manipulator performance measures - a comprehensive literature survey. J. Intell. Robot. Syst. **77**, 1–24 (2014). https://doi.org/10.1007/s10846-014-0024-y

82. Rosyid, A., El-Khasawneh, B., Alazzam, A.: Review article: Performance measures of parallel kinematics manipulators. Mech. Sci. **11**(1), 49–73 (2020). https://doi.org/10.5194/ms-11-49-2020. (https://ms.copernicus.org/articles/11/49/2020/)

83. Murray, R., Li, Z., Sastry, S., Sastry, S.: A mathematical introduction to robotic manipulation (1994)

84. Klein, C.A., Blaho, B.E.: Dexterity measures for the design and control of kinematically redundant manipulators. The Int. J. Robot. Res. **6**(2), 72–83 (1987). https://doi.org/10.1177/027836498700600206

85. Kim, J.-O., Khosla, K.: Dexterity measures for design and control of manipulators. In: Proceedings IROS '91:IEEE/RSJ International Workshop on Intelligent Robots and Systems '91, vol. 2, pp. 758–763 (1991). https://doi.org/10.1109/IROS.1991.174572

86. Wang, J., Wu, C., Liu, X.-J.: Performance evaluation of parallel manipulators: Motion/force transmissibility and its index. Mech. Mach. Theory **45**(10), 1462–1476 (2010). https://doi.org/10.1016/j.mechmachtheory.2010.05.001. (https://www.sciencedirect.com/science/article/pii/S0094114X10000789)

87. Xie, F., Liu, X.-J., Wang, J.: Performance evaluation of redundant parallel manipulators assimilating motion/force transmissibility. Int. J. Adv. Robot. Syst. **8**(5), 66 (2011). https://doi.org/10.5772/50904

88. Patel, V.V., Dollar, A.M.: Robot hand based on a spherical parallel mechanism for within-hand rotations about a fixed point. In: 2021 IEEE/RSJ International Conference on Intelligent Robots and Systems (IROS), pp. 709–716 (2021). https://doi.org/10.1109/IROS51168.2021.9636704

89. Nokleby, S., Fisher, R., Podhorodeski, R., Firmani, F.: Force capabilities of redundantly-actuated parallel manipulators. Mech. Mach. Theory **40**(5), 578–599 (2005). https://www.sciencedirect.com/science/article/pii/S0094114X04001739. https://doi.org/10.1016/j.mechmachtheory.2004.10.005

90. Ozaki, H., Wang, H., Liu, X., Gao, F.: The atlas of the payload capability for design of 2-dof planar parallel manipulators. In: 1996 IEEE International Conference on Systems, Man and Cybernetics. Information Intelligence and Systems (Cat. No.96CH35929), vol. 2, 1483–1488 (1996). https://doi.org/10.1109/ICSMC.1996.571364

91. Wu, J., Wang, J., Wang, L., You, Z.: Performance comparison of three planar 3-dof parallel manipulators with 4-rrr, 3-rrr and 2-rrr structures. Mechatronics **20**(4), 510–517 (2010). https://doi.org/10.1016/j.mechatronics.2010.04.012. (https://www.sciencedirect.com/science/article/pii/S0957415810000802)

92. Feller, D.: Github bytecake. https://github.com/bytecake (2021). Accessed 10 Jan 2021

David Feller received the B.Sc. degree in Mechanical Engineering and the M.Sc. degree in Mechatronics from the Clausthal University of Technology, Clausthal-Zellerfeld, Germany, in 2013 and 2016, respectively. Since 2016, he is working as a Research Assistant in the department of Automation Technology in the Institute of Electrical Information Technology at the Clausthal University of Technology. Currently, he is actively pursuing a Ph.D. degree in Mechanical Engineering, focusing on the ongoing research in the field of legged robots. His research interests primarily revolve around robotics applications including mechanism, manipulator, and controller design.